

## Research

# Hydrothermally derived Cr-doped SnS<sub>2</sub> layered nanoplates: investigation of their controlled structural, morphological, optical, magnetic, photo response and photocatalytic activities

Aparna Paul<sup>1</sup> · I. N. Esha<sup>1</sup> · Rutaba Jania<sup>1</sup> · Sheikh Manjura Hoque<sup>2</sup> · Shirin Akter Jahan<sup>3</sup> · Faria Chowdhury<sup>3</sup> · Kazi Haniun Maria<sup>1</sup>

Received: 6 June 2024 / Accepted: 26 August 2024

Published online: 31 August 2024

© The Author(s) 2024 [OPEN](#)

## Abstract

A facile method has been employed to synthesize pristine and Cr-doped SnS<sub>2</sub> (Cr: SnS<sub>2</sub>) nanoplates (Sn<sub>1-x</sub>Cr<sub>x</sub>S<sub>2</sub>, here x = 0.0, 0.2, 0.4, 0.6, 0.8, and 1.0) and Cr: SnS<sub>2</sub> nanoplates (NPs) were successfully synthesized via hydrothermal method. The nanoplates' structure was hexagonal, with a preference for orientation along the (001) plane; there was no evidence of additional undesirable phases. FTIR and EDX were used to observe the existence of functional groups in the samples where Sn-S bonds were present in each of the produced pristine and Cr: SnS<sub>2</sub> nanoplates. XPS measurements demonstrated the existence of Sn, S, and Cr. FESEM revealed that the morphological properties of the nanoplates included several hexagonal grains. Magnetic characterizations showed that with increasing doping concentration of Cr, SnS<sub>2</sub> nanoplates become superparamagnetic from ferromagnetic. The band gap values for the pristine and Cr: SnS<sub>2</sub> nanoplates calculated from the absorbance spectra decreased from 2.53 to 2.08 eV with an increase in doping concentration. The photoluminescence spectra of the pristine SnS<sub>2</sub> and Cr: SnS<sub>2</sub> nanoplates exhibit two strong emission peaks at around 562 and 666 nm for an excitation wavelength of 420 nm. The Cr: SnS<sub>2</sub> nanoplates have demonstrated the resistive behavior of the sample. The Cr: SnS<sub>2</sub> nanoplates have shown good photocatalytic activity towards the decolorization of rhodamine B under visible irradiation.

## Article highlights

1. Hydrothermally synthesized pristine SnS<sub>2</sub> and Cr: SnS<sub>2</sub> nanoplates exhibit hexagonal crystal structures and the hexagonal shape of layered nanoplates is apparent in both cases.
2. The ferromagnetic order is introduced by Cr doping in SnS<sub>2</sub> which increases the formation of dilute magnetic semiconductors that can therefore be used in spintronic devices.
3. The Sn<sub>0.6</sub>Cr<sub>0.4</sub>S<sub>2</sub> photocatalyst shows the highest photocatalytic activity and a degradation efficiency of 71%, which is 3.4 times higher than the pure SnS<sub>2</sub> catalyst.

**Keywords** Cr: SnS<sub>2</sub> · Nanoplates · Hexagonal grain · Ferromagnetism · Photoluminescence · Photocatalytic activity

✉ Kazi Haniun Maria, kazimaria@du.ac.bd | <sup>1</sup>Department of Physics, University of Dhaka, Dhaka 1000, Bangladesh. <sup>2</sup>Material Science Division, Atomic Energy Centre, Dhaka 1000, Bangladesh. <sup>3</sup>Bangladesh Council of Scientific and Industrial Research (BCSIR), Dhaka 1205, Bangladesh.



## 1 Introduction

In contrast with the past, environmental pollution has become a major threat that also increasing gradually and imposing serious damage on living organisms including human health [1–3]. In the majority of cases, pollutants such as the presence of heavy metals, toxic gases, particulates, organic dye, and other macroscopic pollutants that exist in different forms in nature increase water pollution [4–8]. Therefore, the scientific community has been working to rectify this environmental issue by developing an alternate clean and renewable energy source from the abundance of nature. Among these issues, water pollution caused by waste has agonized researchers due to lack of drinking water, increase of infant mortality by water diseases, disturbance of biodiversity, impurity of food chain etc. Ozonization, carbon adsorption, flocculation, and activated sludge processes have been prevalent in reducing the pollutants from the wastewater. Unfortunately, these methods require expensive tools and also produce secondary pollution [9, 10]. To combat limitations, the photocatalytic degradation process can be used to convert toxic organic pollutants into nontoxic intermediates by irradiating them with visible or ultraviolet light [11, 12].

Nowadays, semiconductor nanomaterials (NMs) based photocatalysts have been extensively used to monitor environmental pollution and manage significant hazards. Semiconductor nanomaterials exhibit modular structure, large surface area, high porosity, high charge transfer, a tunable optical band gap, numerous active sites, and enhanced catalytic activity for detecting heavy metal ions, pesticides, and other toxic pollutants [13–15]. As a result, they can be utilized as photocatalysts for organic dye degradation of polluted wastewater [13]. Till now,  $\text{TiO}_2$ ,  $\text{SnO}_2$ ,  $\text{ZnO}$  semiconducting NMs are the most well-known photocatalysts for their low cost, excellent photocatalytic activity, chemical and photochemical stability, and biocompatibility [16–18]. Yet the search for effective visible light-sensitive photocatalysts is becoming increasingly appealing in this field which may further help to monitor and eliminate environmental pollution [19]. Besides, the improvement of a unique photocatalyst with a high absorption capacity and reduced bandgap needs to be explored to diminish conventional drawbacks such as fewer active sites with high bandgap, less low availability of UV light, and prolonged quantum efficiency [19, 20].

$\text{SnS}_2$ , semiconducting metal sulfides, is a significant class of visible light-active compounds with a tiny band gap, high surface area, and abundant active surface sites [18, 19, 21]. Due to its diverse array of optical and electrical characteristics,  $\text{SnS}_2$  nanostructures have garnered significant attention recently and can serve as solar cells [22], lithium/sodium ion batteries [19], field-effect transistors, optoelectronics [19], photoluminescent materials [18], photodetectors, photocatalysts [13, 23, 24], and sensors [22]. Tin disulfide ( $\text{SnS}_2$ ) is an n-type semiconductor from IV–VI group and belongs to the two-dimensional-layered metal dichalcogenides family with a narrow band gap of 2.18–2.44 eV [13, 23, 24].  $\text{SnS}_2$  exhibits a hexagonal cadmium iodide motif crystal structure in which one layer of a tin atom is sandwiched between two layers of a hexagonal close-packed sulfur atom [13, 23, 24]. The neighboring sulfur monolayer is covalently connected by a feeble Van der Waals force [25–27]. However, several works have been reported on  $\text{SnS}_2$  nanoplate's (NPs) morphology-dependent photocatalytic activity [23, 24, 28–31], it is of utmost importance to increase the degradation efficiency of  $\text{SnS}_2$  NPs photocatalysts. There are a few drawbacks such as high bandgap, less active sites, and low availability (3–5%) of UV light which reduces the photocatalytic activity of the  $\text{SnS}_2$  NPs photocatalyst. Foreign ion doping into  $\text{SnS}_2$  develops a new photocatalyst with a high absorption capacity that can reduce the bandgap and override the drawbacks [28–31]. Due to the presence of wide interlayer spacing inside the  $\text{SnS}_2$  structure, doping of foreign ions can enhance the photocatalytic activity of  $\text{SnS}_2$  in the degradation of aqueous colorants under ultraviolet light [32, 33].

The photocatalytic activity is found to increase with the doping of cerium. However, the large variation of ionic distance between  $\text{Ce}^{3+}$  (102 Å) and  $\text{Sn}^{4+}$  (0.71 Å) disturbs the lattice order inside the crystal [34]. Therefore, the doped ions should have ionic radii close to those of  $\text{Sn}^{4+}$  ions. There are several reports such as  $\text{Mg}^{2+}$  (0.72 Å) [35],  $\text{Ni}^{2+}$  (0.69 Å) [36],  $\text{In}^{3+}$  (0.81 Å) [37],  $\text{Co}^{2+}$  (0.89 Å) [38],  $\text{V}^{3+}$  (0.64 Å) [39] and  $\text{Cr}^{3+}$  (0.62 Å) [13, 40, 41] doped  $\text{SnS}_2$  which can enhance room temperature ferromagnetism and the photocatalytic activity of the pristine  $\text{SnS}_2$ . However, to the best of our knowledge, no systematic study has been performed to observe the effect of Cr doping on the magnetic and photocatalytic properties of  $\text{SnS}_2$  nanoplates simultaneously. Therefore, it is important to understand the magnetic and optical origin of Cr-doped  $\text{SnS}_2$  which is required for producing high-speed energy-saving electronic equipment in the future [42]. In this context,  $\text{Cr}^{3+}$  (0.62 Å) is selected because its radius is close to  $\text{Sn}^{4+}$  (0.71 Å). The doped  $\text{Cr}^{3+}$  ion replaces the  $\text{Sn}^{4+}$  ions and creates an intermediary band inside the band gap of the  $\text{SnS}_2$  compound [40]. This intermediary band sets up an additional energy state that can improve the absorption of photons in the visible region and effectively encourage the segregation of photogenerated electron–hole combinations, leading to greater participation of light-induced electrons in the photocatalytic process. Besides antiferromagnetic  $\text{Cr}^{3+}$  with its  $3d^3$  high-spin configuration creates large magnetic

moments in the host  $\text{SnS}_2$  semiconductor nanoplates [41], developing dilute magnetic semiconductors (DMSs). Dilute magnetic semiconductors exploit both semiconducting and magnetic properties by utilizing the charge and spin of electrons and fastening the performance of electronic devices. The level of Cr doping also affects the magnetic properties of the DMSs. Therefore, the novelty of the investigation is to explore this room-temperature ferromagnetism with controllable semiconducting properties of  $\text{SnS}_2$  which will be key materials for developing spintronic devices [42].

Different techniques have been used for the synthesis of pure  $\text{SnS}_2$  and Cr:  $\text{SnS}_2$  nanoplates (NPs) such as sonochemical [43], hydrothermal [44], solvothermal [26], and laser ablation procedures [25]. Among all the methods, the hydrothermal reaction approach is the most appropriate of the documented synthesis methods for producing nanostructured materials with the required morphology and shape. Also, it is easier to use, less hazardous, safe for the environment, affordable and produces a significant yield [44, 45]. Hence, this work reports the hydrothermal synthesis process that produces hexagon-shaped  $\text{SnS}_2$  nanoplates with varying Cr doping concentrations. Several analytical techniques were employed, including X-ray diffraction (XRD), Fourier Transform Infrared Spectroscopy (FTIR), Scanning Electron Microscopy (SEM), Energy-Dispersive Spectroscopy (EDS), High-Resolution Transmission Electron Microscopy (HRTEM), X-ray Photoelectron Spectroscopy (XPS), Vibrating-Sample Magnetometer (VSM), Ultraviolet-visible (UV-Vis) spectroscopy, and Photoluminescence (PL) methods to explore the effect of Cr doping on the  $\text{SnS}_2$  nanoplates. Additionally, the photocatalytic performance of these nanoplates was also performed under UV-visible light irradiation. Measurements of photoconductivity and the degradation of RhB dye were also conducted on the sample. To enhance the photocatalytic degradation ability of  $\text{SnS}_2$ , a photosensitization effect has been employed which expanded the visible light absorption through excitation of the rhodamine B (RhB) sensitizer followed by charge transfer to the semiconductors [13]. The electron transfer among the photosensitizers, semiconductors, and reactive intermediates normally depends on the structure and morphology of photocatalysts [13, 23, 24]. It was known that a 2D  $\text{SnS}_2$  nanostructured semiconductor exhibits highly reactive photocatalysis for RhB degradation through a photosensitization process [13, 23, 24, 28]. Therefore, another attempt of this study was to control the shape of the Cr-doped nanoplate by optimizing synthesis conditions. In our study, the photosensitized degradation of RhB was found to be raised by the synergistic effect of the RhB and 2D  $\text{SnS}_2$  nanoplates. A hexagonal layered nanoplates formation mechanism has been proposed by monitoring the structural evolution with Cr doping using the electron microscope. In addition, the characterization results affirm that Cr:  $\text{SnS}_2$  can replace toxic CdS as substituted Cr minimizes the imbalance between the absorber and the window layer in photovoltaic applications.

## 2 Experimental

### 2.1 Materials

Stannic (IV) chloride pentahydrate ( $\text{SnCl}_4 \cdot 5\text{H}_2\text{O}$ , 98% pure), thioacetamide ( $\text{C}_2\text{H}_5\text{NS}$ , 98% pure) were procured from Merck Inc, India. Chromium (III) chloride hexahydrate ( $\text{CrCl}_3 \cdot 6\text{H}_2\text{O}$ , 98% pure) were purchased from Sigma-Aldrich (Europe). Concentrated hydrochloric acid (HCl, 37% pure) and Rhodamine B ( $\text{C}_{28}\text{H}_{31}\text{ClN}_2\text{O}_3$ , 98% pure) were purchased from Sisco Research Laboratories (SRL), India. All the chemicals were of analytical grade and were used without any purification.

### 2.2 Sample preparation method

Stannic chloride pentahydrate ( $\text{SnCl}_4 \cdot 5\text{H}_2\text{O}$ ), thioacetamide ( $\text{C}_2\text{H}_5\text{NS}$ ), chromium chloride hexahydrate ( $\text{CrCl}_3 \cdot 6\text{H}_2\text{O}$ ) was used as reagents, and distilled water was used as a solvent to prepare the samples. Concentrated hydrochloric acid (HCl) was used to assist the fast hydrolysis of the reagents and rapid material preparation in a very short time. Here, 0.7513 gm (0.01 mol) thioacetamide ( $\text{C}_2\text{H}_5\text{NS}$ ), 2 ml HCl, and 48 ml distilled water were used, and the amount remained fixed for the preparation of all six samples. The six samples were prepared by varying stannic chloride pentahydrate ( $\text{SnCl}_4 \cdot 5\text{H}_2\text{O}$ ) and chromium chloride ( $\text{CrCl}_3 \cdot 6\text{H}_2\text{O}$ ). All the chemicals were weighed stoichiometrically according to the chemical formula,  $\text{Sn}_{1-x}\text{Cr}_x\text{S}_2$ . In a 100 ml beaker, all the reagents were dissolved, and the solution was continuously stirred for an hour. After that, the solution was taken into a 100 cc Teflon-lined stainless-steel autoclave. The filled autoclave was put into an oven, heated at 200 °C for 24 h, and then was allowed to cool naturally. The precipitation was collected from the Teflon tube, washed three times with DI water, and subsequently dried

at 60 °C in a hot air oven for 12 h for later use. A schematic diagram of sample preparation to get a burned orange powder is shown in Fig. 1.

## 2.3 Characterization technique

The Philips X-pert pro-X-ray diffraction equipment with monochromatic  $\text{CuK}_\alpha$  radiation at a wavelength ( $\lambda$ ) of 0.1540 nm was used to examine the structural identity of the produced pristine and Cr:  $\text{SnS}_2$  NPs. The detected data were taken in a  $2\theta$  range of  $10^\circ$  to  $80^\circ$ . The FTIR analysis spectra were recorded with the Shimadzu IR-Prestige 21, within the spectral range of  $400\text{--}4000\text{ cm}^{-1}$ . The morphology of NPs was examined in detail by using field-emission scanning electron microscopy (FESEM, JSM-7600F, JEOL, Peabody, Massachusetts, USA) with a high vacuum at 15-kV accelerating voltage and a transmission electron microscope (TEM, Talos 200X) at 200 kV operating voltage, respectively. Using Image J software, the average of about 60 grains from the corresponding composition was used to calculate the grain size. Energy dispersive spectroscopy (EDS) analysis was performed to ascertain the composition of pristine and Cr:  $\text{SnS}_2$  NPs. The elemental analysis of the NPs was investigated using X-ray photoelectron spectroscopy (XPS, ULVAC-PHI 5000) with an Al  $\text{K}_\alpha$  X-ray source (1486.6 eV), usually set at 3 kV, 24 W, and an angle of  $45^\circ$ . The absorbance and transmittance spectra of the prepared NPs powder were examined using UV-visible diffuse reflectance spectroscopy (UV-DRS), which was utilized to run over a wavelength range of  $400\text{--}700\text{ nm}$ . The electrical conductivity of the NPs was determined using a homemade two-point probe. The photoluminescence measurements were carried out using a Perkin Elmer spectrofluorometric LS-55 attached to a Xenon lamp.

### 2.3.1 Photocatalytic activity measurement

To examine the photocatalytic properties of  $\text{Sn}_{1-x}\text{Cr}_x\text{S}_2$  ( $x=0, 0.2, 0.4, 0.6$ ), visible light irradiation was used to photocatalytically decolorize Rhodamine B (RhB, SRL, India) at room temperature. A 100W halogen lamp was employed as a source of artificial sunlight to test the samples' photocatalytic activity. A standard procedure involved adding 20 mg of catalyst to 100 mL of RhB aqueous solution ( $C_0 = 5\text{ mg/L}$ ). For roughly 30 min, the dispersions were left in the dark to create an equilibrium between adsorption and desorption. Almost 5 mL of the irradiation suspensions were removed and centrifuged to eliminate the catalyst at the designated intervals. With the support of a UV-Vis Spectrophotometer (Shimadzu UV 1900i), the residue from the solutions was investigated. The equation  $\eta = (C_0 - C_t)/C_0 \times 100\%$  defines the photocatalytic decolorization efficiency, where  $C_0$  represents the starting concentration of RhB and  $C_t$  denotes the concentration of RhB following light irradiation.

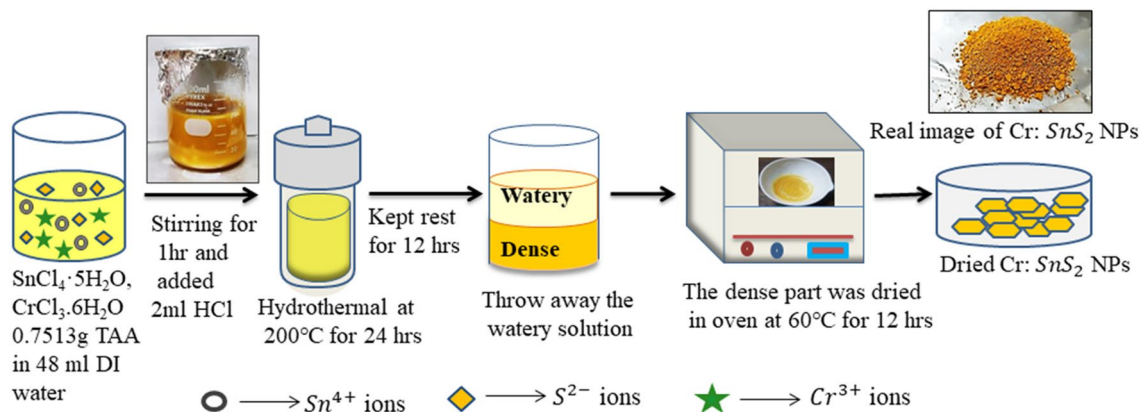


Fig. 1 Schematic diagram of pristine and Cr:  $\text{SnS}_2$  nanoplates (NPs) via hydrothermal method

### 3 Results and discussion

#### 3.1 Growth mechanism

The formation of Cr: SnS<sub>2</sub> NPs comprises various phases and the quality of NPs depends on the optimization of reagent dissociation during hydrolysis. In this study, stannic ions initially combine with HCl acid to form a complex and hasten the dissociation of thioacetamide. Thioacetamide breakdown at ambient temperature results in H<sub>2</sub>S, which subsequently breaks down to produce S<sup>2-</sup> ion. In the end, the Sn<sup>4+</sup> ion and S<sup>2-</sup> ion combine to form SnS<sub>2</sub> [45]. The dissociation of thioacetamide at room temperature slowly releases sulfur ions influencing the nucleation and growth of NPs. Therefore, these slowly released sulfur ions have delayed the nucleation, and a longer growth time was required to form SnS<sub>2</sub> nanoplates with smaller sizes. To introduce the Cr<sup>3+</sup> ion, chromium chloride (CrCl<sub>3</sub>·6H<sub>2</sub>O) has been used which forms a complex [Cr(H<sub>2</sub>O)<sub>6</sub>]Cl<sub>3</sub> when placed in water. Then the SnS<sub>2</sub> might combine with that complex and form the Sn<sub>1-x</sub>Cr<sub>x</sub>S<sub>2</sub> by substituting Cl with H<sub>2</sub>O. As the reaction proceeds, the formed plates assemble to form a hexagonal structure. During the procedure, two drops of HCl were used to regulate the pH of the solution. Later, the solution was washed with distilled water to eliminate any extra HCl acid. The schematic of the proposed growth mechanism of the pristine and Cr-doped SnS<sub>2</sub> NPs formation is shown in Fig. 2. The chemical reactions for the process of synthesizing Sn<sub>1-x</sub>Cr<sub>x</sub>S<sub>2</sub> may be as follows:

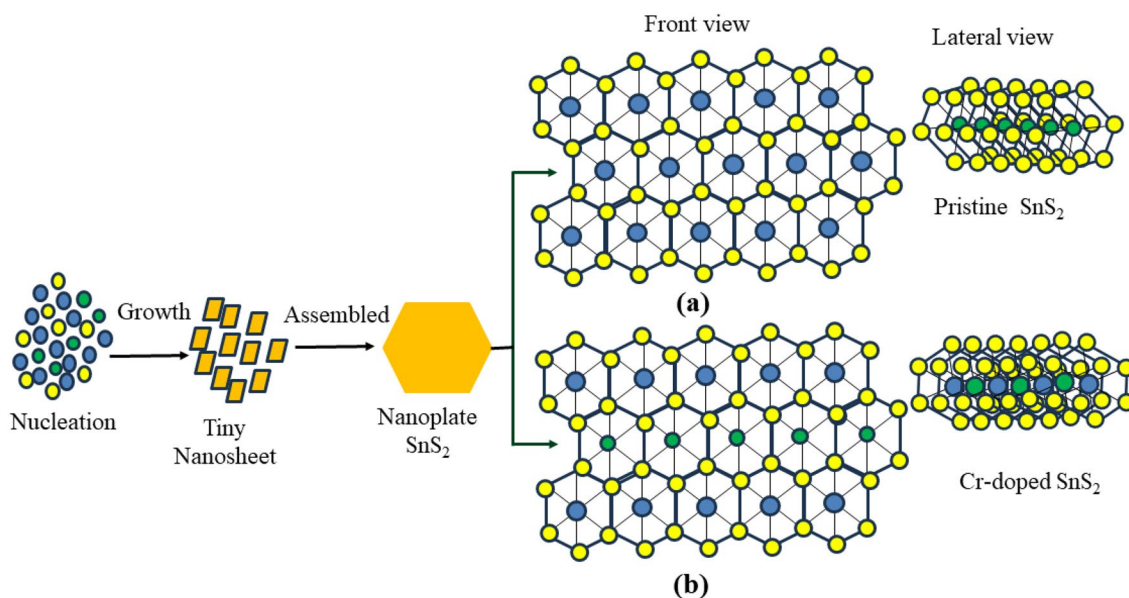
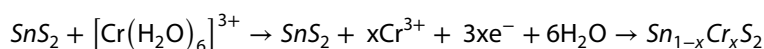
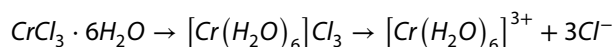
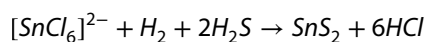
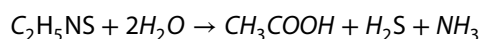
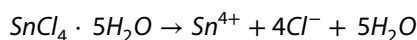


Fig. 2 Schematic diagram of the proposed mechanism of the **a** pristine and **b** Cr: SnS<sub>2</sub> nanoplates

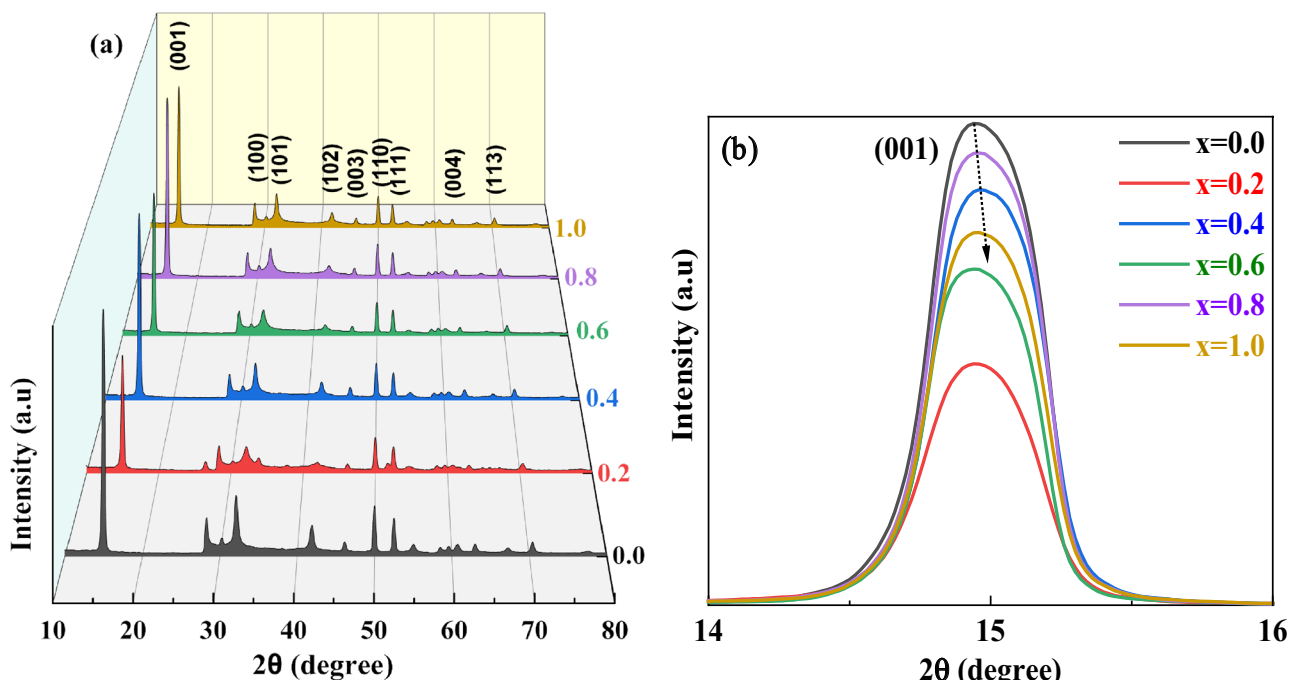


Fig. 3 **a** XRD patterns; **b** Magnified image of (001) peak of SnS<sub>2</sub> and Cr: SnS<sub>2</sub>

**Table 1** Lattice parameters and *c/a* ratio of SnS<sub>2</sub> and Cr: SnS<sub>2</sub> NPs

| Cr concentration (at %) | <i>a</i> (Å) | <i>c</i> (Å) | <i>c/a</i> |
|-------------------------|--------------|--------------|------------|
| 0                       | 3.63         | 5.84         | 1.60       |
| 0.2                     | 3.65         | 5.82         | 1.59       |
| 0.4                     | 3.64         | 5.89         | 1.61       |
| 0.6                     | 3.59         | 5.81         | 1.62       |
| 0.8                     | 3.64         | 5.79         | 1.59       |
| 1.0                     | 3.62         | 5.81         | 1.60       |

### 3.2 X-ray diffraction analysis

The X-ray diffraction patterns of pristine SnS<sub>2</sub> and Cr: SnS<sub>2</sub> NPs produced by the hydrothermal method with various Cr concentrations (0.2, 0.4, 0.6, 0.8, 1 at %) are shown in Fig. 3a. Several intense peaks are seen in the diffraction pattern for the NPs at 14.83°, 28.25°, 32.23°, 41.81°, 46.03°, 52.48°, 62.93°, and 70.51°, which correspond to (001), (100), (101), (102), (110), (111), (004), and (113) crystal planes of SnS<sub>2</sub> hexagonal phase (JPCDS No. 23-0677), respectively. The doping of the Cr element does not change the crystal structure of SnS<sub>2</sub>. No additional Cr sulfide peaks are observed in the XRD pattern. The XRD patterns of 0.2 at% Cr doping show peaks with less intensities compared to other Cr: SnS<sub>2</sub> NPs. The decrease in peak intensity can be attributed to the deterioration of crystalline quality [46, 47]. From the magnified image of the (001) peak in Fig. 3b, it is noticeable that metal (Cr) doped in crystal lattice exhibits a modest shift to higher scattering angles. Moreover, it can be seen from Table 1 that the lattice parameter has been changed slightly due to variation of the stress between the ions.

### 3.3 FTIR analysis

Figure 4a illustrates the results of an FTIR investigation of SnS<sub>2</sub> and Cr: SnS<sub>2</sub> NPs in the 400–4000 cm<sup>-1</sup> wavenumber range. The O–H bond vibration is represented by the peak that can be seen at 3446 cm<sup>-1</sup> and it possibly has been

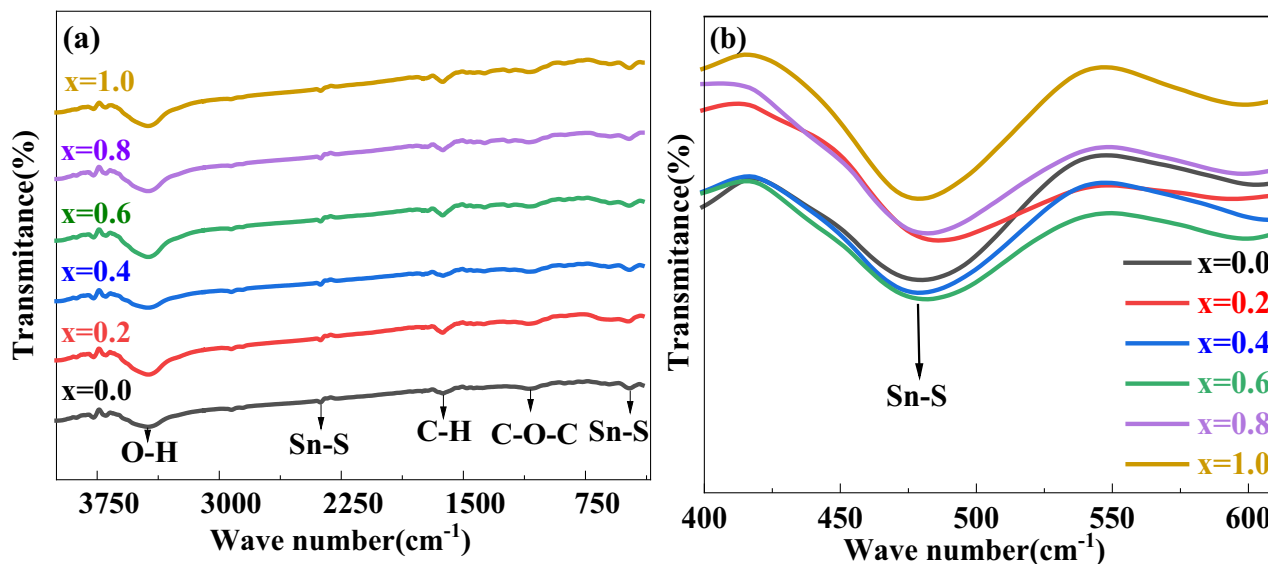


Fig. 4 FTIR spectra of **a** SnS<sub>2</sub> and Cr: SnS<sub>2</sub> NPs **b** magnified image of Sn–S bond

caused by the surface hydroxyls and adsorbed water [48]. The creation of the Sn–S stretching bond is thought to be responsible for the bands seen in spectra in the wavenumber range 2200–2500 cm<sup>-1</sup>. A peak at 1625.3 cm<sup>-1</sup> represents the C–H bond which possibly comes from thioacetamide [49]. The presence of the carboxylic group (C–O–C) is represented by the peak that was observed at 1078 cm<sup>-1</sup>. All of the samples showed the presence of a peak at 474 cm<sup>-1</sup> that was associated with the Sn–S bond. Since Cr–S stretching only manifests itself below 400 cm<sup>-1</sup> [50], there isn't a peak due to Cr visible in the doped samples. With an increase in the Cr doping concentration, the sample's corresponding peak orientation does not change, which is also consistent with the XRD data, showing that Cr<sup>3+</sup> was effectively integrated into the SnS<sub>2</sub> lattice. This absorption peak indicates that all SnS<sub>2</sub> and Cr: SnS<sub>2</sub> NPs displayed a symmetric stretching mode of hexagonal structure.

The stretching frequency for the Sn–S bond is 475.2 cm<sup>-1</sup> for pure SnS<sub>2</sub> which is shifted to a higher frequency of 486.5 cm<sup>-1</sup> for 0.2 at% Cr doping (Fig. 4b). Since 0.2 at% Cr: SnS<sub>2</sub> NPs is lighter than pristine SnS<sub>2</sub>, hence peak shift is towards the higher wave number side. Also, the frequency of vibration is inversely proportional to the mass of the vibrating molecule. So lighter the molecule, the higher the vibration frequency and the higher the wave numbers [51].

### 3.4 XPS study

The XPS analysis of Sn<sub>4.6</sub>Cr<sub>0.4</sub>S<sub>2</sub> nanoplates was performed on Si (100) wafer in the binding energy range of 0 ~ 1300 eV to investigate the electronic states of Sn, S, and Cr elements. The survey spectrum of Fig. 5a shows the multiple peaks, including S 2s, S 2p, Sn 3s, Sn 3p, Sn 3d, Sn 4d, and Cr 2p proving that the produced nanoplates incorporate Sn, S, and Cr elements. The C 1s peak at 284.6 eV can be attributed to adventitious carbon which was detected for the surface contamination [52]. The O 1s peak centered at 531.49 eV originated from the oxygen-deficient regions of the glass substrate [53]. Figure 5b shows that the Sn 3d doublet exhibits two signals at 486.2 and 494.6 eV corresponding to the Sn 3d<sub>3/2</sub> and Sn 3d<sub>5/2</sub> indicating that Sn exists in the Sn<sup>4+</sup> oxidation state, respectively. In Fig. 5c, two peaks with binding energies of 161.68 eV and 162.88 eV in the S 2p basic level are observed corresponding to the S 2p<sub>3/2</sub> and S 2p<sub>1/2</sub> which confirm that S atoms in the SnS<sub>2</sub> valence state. The binding energy values observed for Sn 3d and S 2p spectra are in good agreement with Sn<sup>4+</sup> and S<sup>2-</sup> of SnS<sub>2</sub> [53, 54]. Figure 5d shows that a strong peak appeared at 577.02 eV corresponding to Cr 2p<sub>3/2</sub> which demonstrates that Cr is present in the valence of Cr<sup>3+</sup> ions [54].

### 3.5 FESEM analysis

The morphology, structure, and EDX characterizations of the synthesized Cr: SnS<sub>2</sub> NPs are investigated with FE-SEM as shown in Fig. 6. The image of pristine SnS<sub>2</sub> (Fig. 6a) and Cr: SnS<sub>2</sub> (Fig. 6b–f) NPs display hexagonal-like nanosheets with smooth, vertically interconnected surfaces. The scanned area is nicely covered with a significant number of

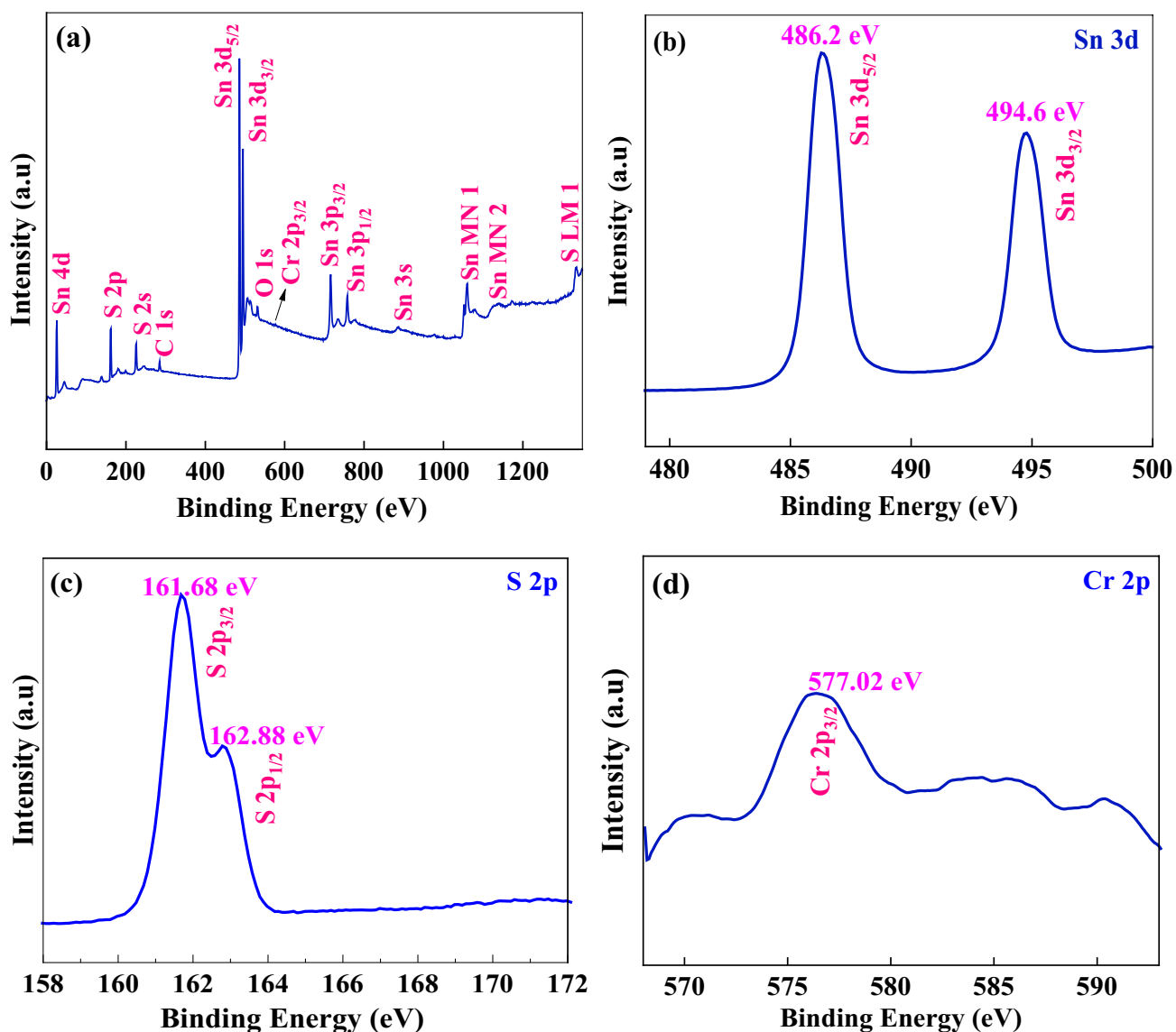


Fig. 5 XPS survey of **a** 0.4 at% Cr: SnS<sub>2</sub>; **b** Sn 3d; **c** S 2p; **d** Cr 2p of 0.4 at% Cr: SnS<sub>2</sub>

small grains in hexagonal form and shows a compact and dense uniform surface. The size and thickness of the observed 2D nanosheets are around ~ 200 nm and 5 to 10 nm, respectively. It is found that the Cr doping sample possesses some spherical particles along with hexagonal sheets. As the mole percentage of Cr increases, the particle size becomes larger and agglomerates which consist also a mixture of more fine grains with sizes in the range 140 to 340 nm in diameter (inset of Fig. 6a–f). The particle size of the Cr-doped sample is larger, that is about 17.92 nm. The grain size from the FESEM image is determined by the distance between the discernible grain boundaries, which is greater than the grain size determined from XRD peaks because the XRD method analyzes the evolution of the crystals which leads to smaller grains [55].

In Fig. 7a–c, the layered structure of SnS<sub>2</sub> and Cr: SnS<sub>2</sub> is significantly apparent. The elongated shape of the particles has also been observed in pristine SnS<sub>2</sub> and Cr: SnS<sub>2</sub> NPs where the nanoplates are thicker and more closely spaced. Therefore, this layer can be exfoliated down to a single hexagonal nanosheet which is expected to have better electron transport properties.



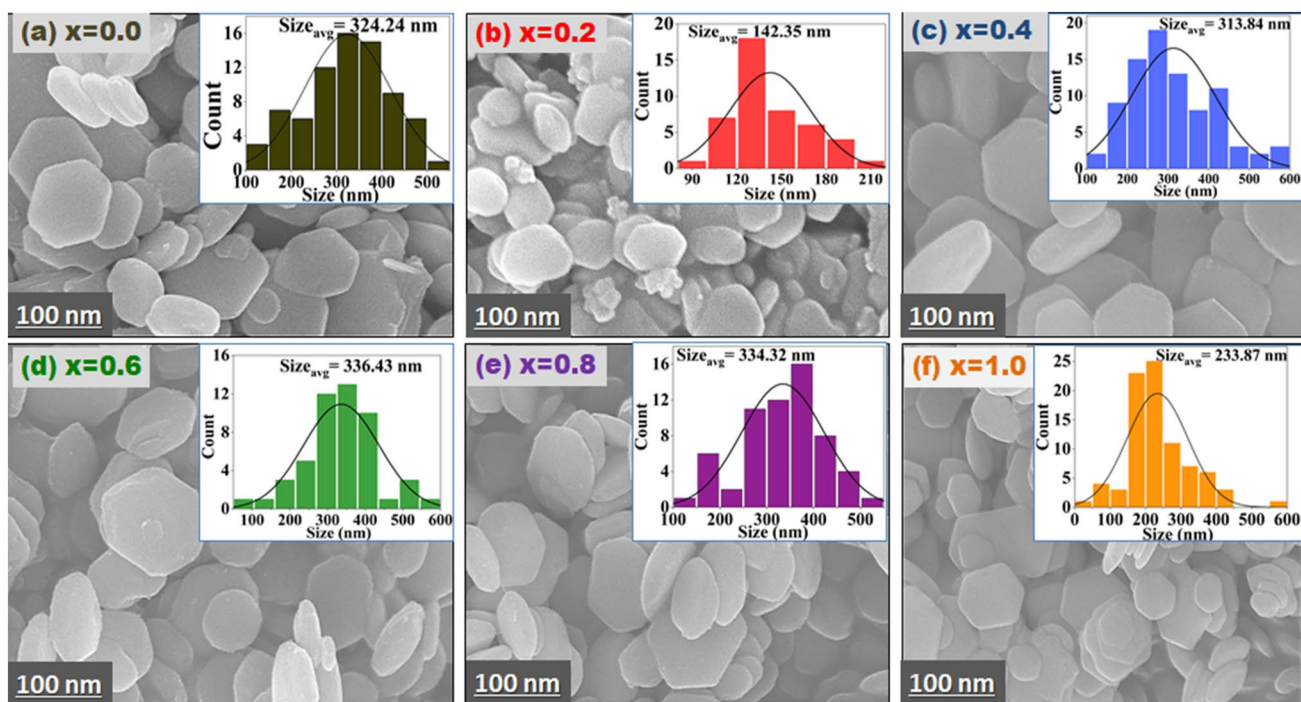


Fig. 6 FESEM micrographs **a**  $\text{SnS}_2$ , **b** 0.2, **c** 0.4, **d** 0.6, **e** 0.8 and **f** 1.0 at% Cr:  $\text{SnS}_2$  NPs. Inset shows FESEM micrographs with grain size

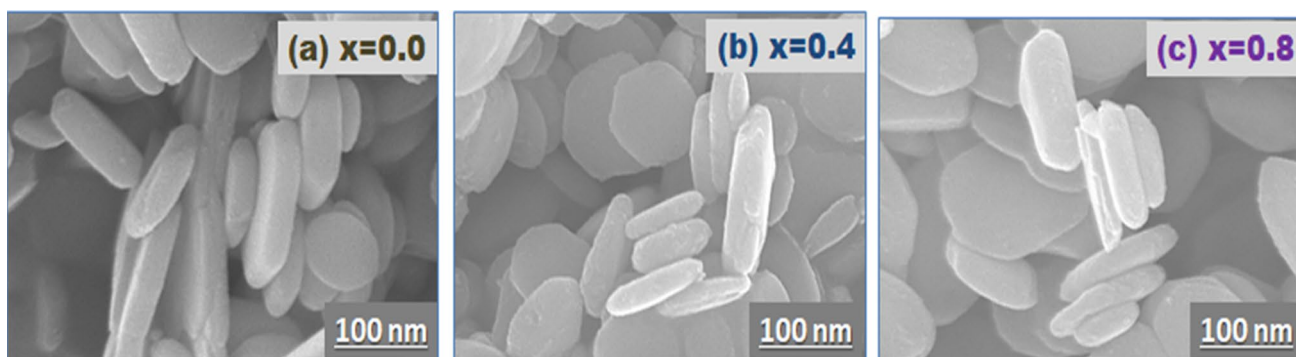
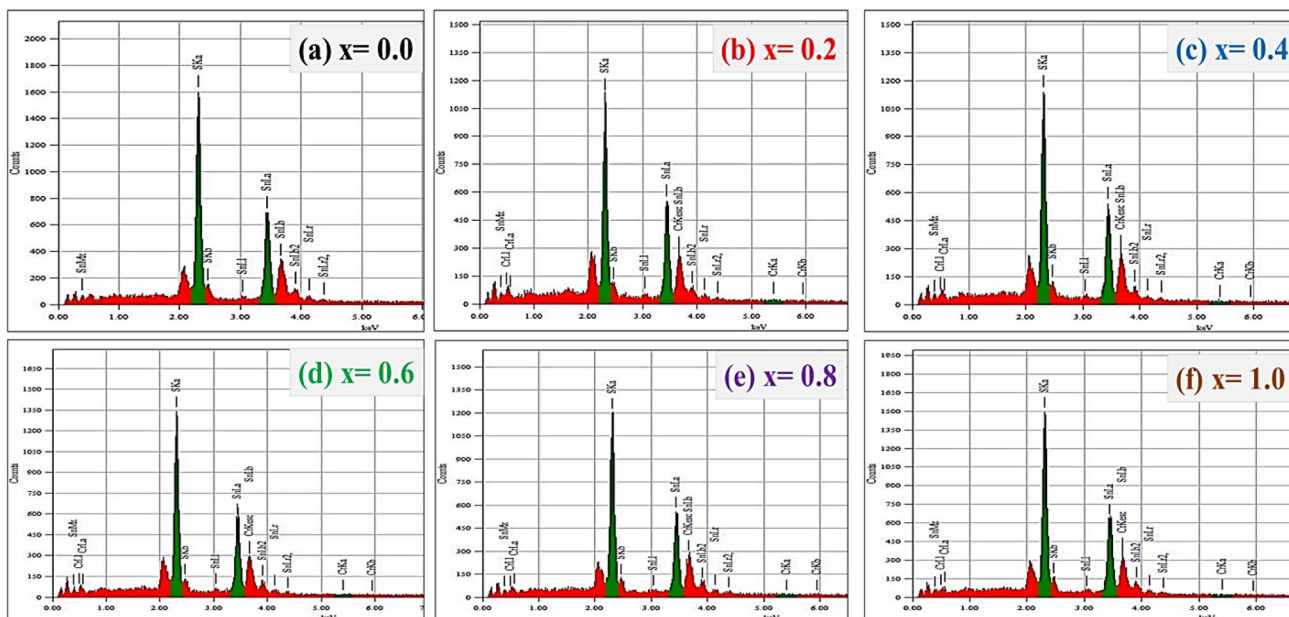


Fig. 7 FESEM micrographs show the elongated shaped particles of pristine **a**  $\text{SnS}_2$ , and **b** 0.4, and **c** 0.8 at% Cr:  $\text{SnS}_2$  NPs

### 3.6 EDX analysis

Figure 8a–f shows the EDX spectra of pristine  $\text{SnS}_2$  and Cr:  $\text{SnS}_2$  NPs. The EDS spectra confirm the presence of tin, sulfur in the pristine, and Cr in all the doped samples. No impurity peaks corresponding to other elements are detected, indicating the purity of the nanoplates.

Table 2 provides a quantitative analysis of the elements present in the samples. The weight percentage data shows that Cr:  $\text{SnS}_2$  NPs are slightly rich in tin content. The atomic ratio, S/Sn in Cr:  $\text{SnS}_2$  NPs decreases with increasing doped Cr concentration due to the creation of  $\text{Sn}^{4+}$  vacancies as a certain amount of  $\text{Sn}^{4+}$  ions are substituted by Cr [56]. A modest drop in S content is also observed with the Cr addition. The delayed dissociation of thioacetamide in the solution may be connected to the S deficiency [57, 58].



**Fig. 8** EDS spectra of pristine **a** SnS<sub>2</sub>, and doped **b** 0.2, **c** 0.4, **d** 0.6, **e** 0.8 and **f** 1.0 at% Cr: SnS<sub>2</sub>

**Table 2** The EDX analysis of pristine SnS<sub>2</sub> and Cr: SnS<sub>2</sub> NPs

| Cr concentration (at %) | Elements              |       |      | S/Sn |
|-------------------------|-----------------------|-------|------|------|
|                         | Sn                    | S     | Cr   |      |
|                         | Atomic percentage (%) |       |      |      |
| 0                       | 33.60                 | 66.40 | –    | 1.97 |
| 0.2                     | 35.35                 | 64.46 | 0.19 | 1.82 |
| 0.4                     | 33.65                 | 65.74 | 0.61 | 1.95 |
| 0.6                     | 34.28                 | 65.37 | 0.35 | 1.91 |
| 0.8                     | 34.39                 | 65.55 | 0.26 | 1.90 |
| 1.0                     | 33.96                 | 66.80 | 0.24 | 1.89 |

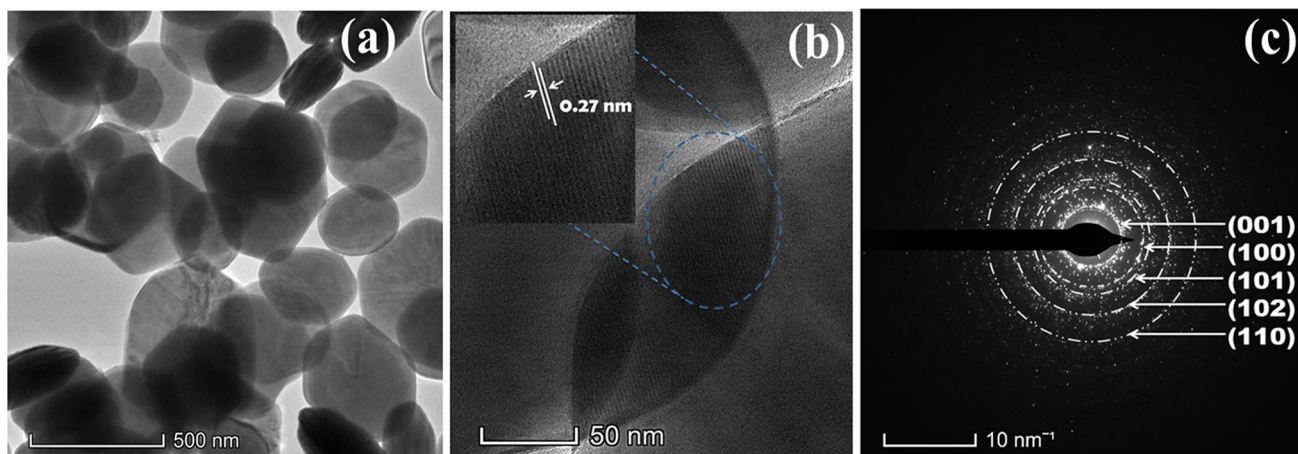


**Fig. 9** HRTEM images of 0.6 at% Cr: SnS<sub>2</sub> NPs

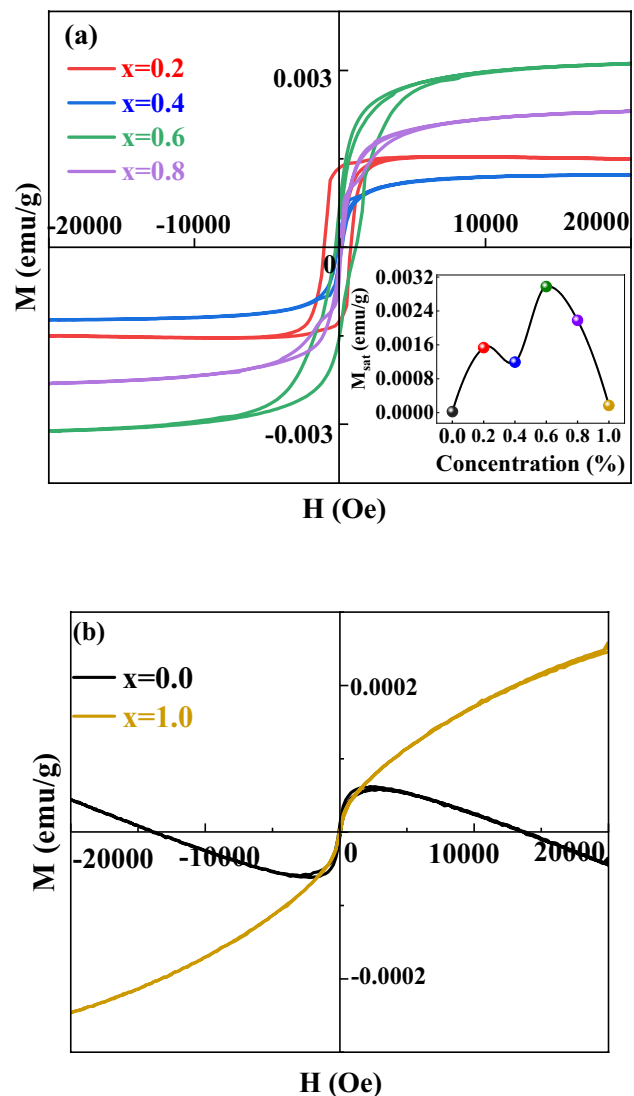
### 3.7 TEM analysis

The HRTEM images of the 0.6 at% Cr doped sample are displayed in Fig. 9a. The Hexagonal-shaped plates having a size in the range of 140–340 nm have been noticed which is consistent with the FESEM images. Figure 9b displays the interplanar spacing of  $d = 0.27$  nm corresponding to (101) planes of Cr: SnS<sub>2</sub> nanoplates. In the SEAD (selective area electron diffraction) image (Fig. 9c), the observed diffraction spots can be indexed as (101), (111), and (100) planes confirming the principal exposed facets of hexagonal Cr: SnS<sub>2</sub>. Overall, the TEM examination supports the creation of extremely crystalline Cr: SnS<sub>2</sub> nanoplates and validates the XRD findings. The regular arrangement, obvious rules, diffraction spots, and defect-free structure of 0.6 at% Cr doped sample seem to indicate that they are single crystals with good crystallinity.

### 3.8 Magnetic properties analysis

Figure 10a displays the magnetization ( $M$ ) as a function of magnetic field ( $H$ ) at room temperature for undoped and Cr: SnS<sub>2</sub> NPs in the magnetic field range of  $-20,000$  to  $20,000$  Oe. Magnetic measurement (Fig. 10b) confirms that pristine SnS<sub>2</sub> exhibits diamagnetism due to a saturated electronic structure [59, 60]. A complete two-dimensional structure of SnS<sub>2</sub> produces lattice fluctuation which also indicates that the sample had fewer intrinsic defects such as cation–anion vacancy, interstitial atom, and bound state which might implant paramagnetism and ferromagnetism into a two-dimensional SnS<sub>2</sub>

**Fig. 10** **a** Field dependences of the magnetization of Cr: SnS<sub>2</sub> NPs measured at Room temperature. The inset shows Cr content dependence of the magnetization. **b** The magnetization curve of pristine SnS<sub>2</sub> and 1.0 at% of Cr: SnS<sub>2</sub> NPs



structure. However,  $\text{SnS}_2$  shows weak ferromagnetism by doping in previous reports [61, 62] as doping produced more vacancies in the samples which increased the ferromagnetism at room temperature. In the case of antiferromagnetic Cr doping, the magnetization in  $\text{SnS}_2$  is observed to enhance, demonstrating that ferromagnetic interaction exists between Sn and Cr ions. XPS analysis reveals the presence of trivalent  $\text{Cr}^{3+}$  ions which exhibit a  $3d^3$  high-spin configuration and it creates magnetic moment in the host  $\text{SnS}_2$ . The inset of Fig. 10a shows that 0.6 at% Cr doping shows the magnetization of  $0.003 \text{ emu g}^{-1}$ , which decreases with a further increase of Cr dopant. This increase in magnetization may be due to the magnetic moment caused by Sn vacancy which in turn creates intrinsic magnetic moment. In addition to these vacancies, it is conjectured that  $\text{Cr}^{3+}$  ions enter the  $\text{SnS}_2$  lattice and substitute  $\text{Sn}^{4+}$  ions which produce vacancies and are related to the enhancement of magnetization [63]. It is concluded that 1.0 at% of Cr doping leads to the formation of superparamagnetic clusters (Fig. 10b) due to the vacancies induced from the majority of Cr atoms in the lattice. These results demonstrate that Cr dopant has induced the ferromagnetic order of intrinsic  $\text{SnS}_2$  at room temperature, known as Dilute magnetic semiconductors, and has potential application in spintronic devices [42].

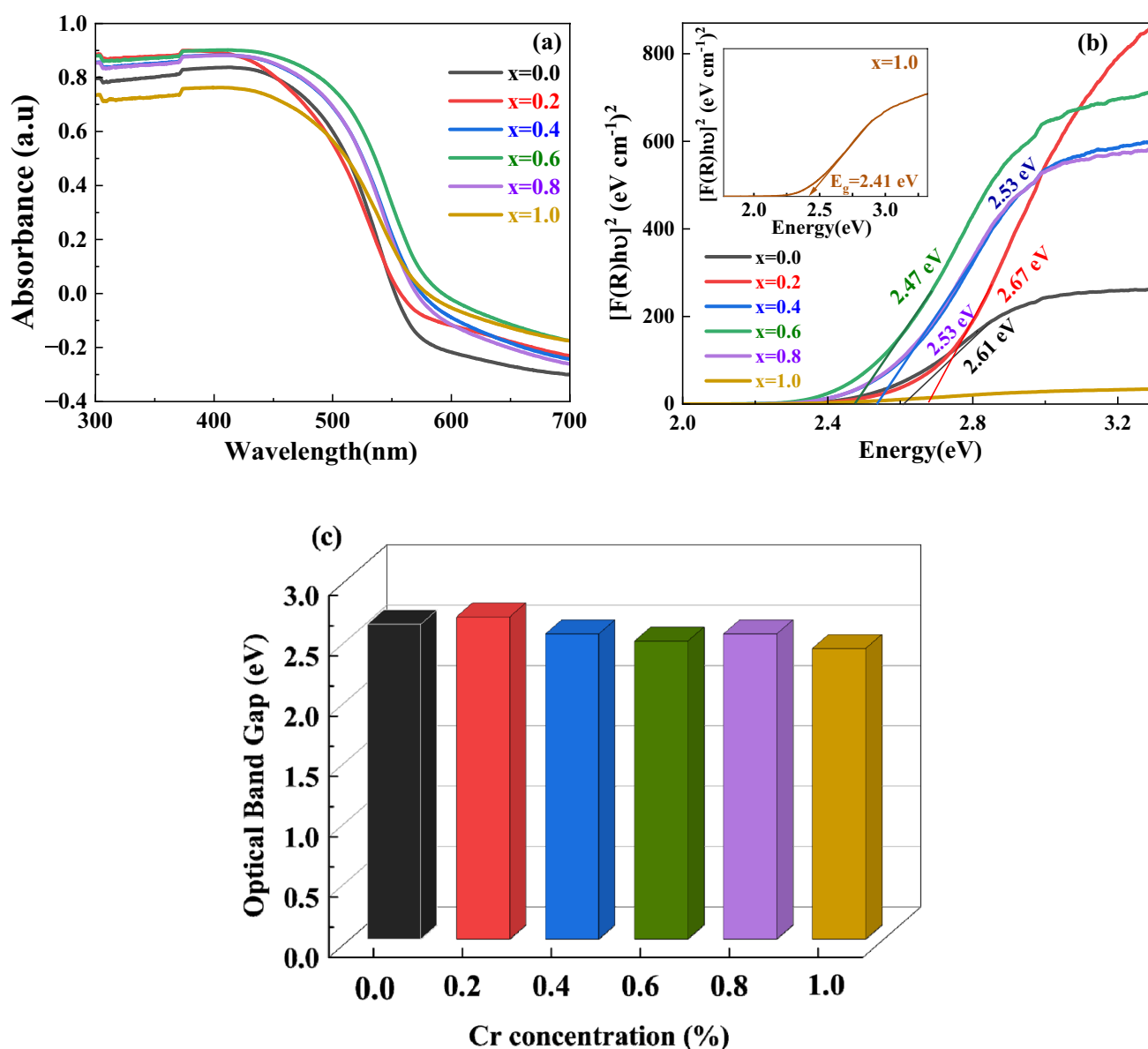


Fig. 11 **a** UV absorbance spectra **b** The band gap for the direct transition of  $\text{SnS}_2$  and Cr:  $\text{SnS}_2$  NPs **c** Bar diagram of band gap vs Cr content

### 3.9 UV–visible diffuse reflectance spectroscopy (UV–vis-DRS) analysis

UV–vis-DRS of the as-synthesized pristine  $\text{SnS}_2$  and Cr:  $\text{SnS}_2$  with different Cr concentrations measured in the wavelength range of 300 to 700 nm are shown in Fig. 11a to evaluate their band gap as well as photo-absorption behavior. All the samples exhibit absorption edge across the whole visible light spectrum and are observed to fall between 400 to 700 nm. This broad absorption spectrum in the visible region demonstrates that the synthesized  $\text{SnS}_2$  and Cr:  $\text{SnS}_2$  NPs could provide good visible light-responsive photocatalysts for degrading organic contaminants. With increasing doping concentration, all samples' transmittance in the visible and near-infrared wavelengths decreases. The reduction in transmittance with increasing doping concentration manifests an increase in absorbance for that specific number of times [64]. The optical absorptions of the samples are observed to increase with wavelength starting at 370 nm and subsequently start to decrease with wavelength. This drop in absorption indicates the existence of an optical band at a particular wavelength.

The band gaps for the direct transition of  $\text{SnS}_2$  and Cr:  $\text{SnS}_2$  NPs are calculated by Tauc's relation and displayed in Fig. 11b. Figure 11c shows that the optical bandgap of pure  $\text{SnS}_2$  is decreased by the  $\text{Cr}^{3+}$  ion doping. At 2% doping, the optical band gap increases, then decreases and a significant blue shift of the band gap is observed. This can happen when some of the  $\text{Sn}^{4+}$  (0.71 Å) in the lattice has been replaced by  $\text{Cr}^{3+}$  (0.63 Å) as a result of the direct energy transfer from the semiconductor excited state to the 3d energy level of  $\text{Cr}^{3+}$  [40, 41]. This demonstrates that the band gap can be tuned by changing the Cr dopant concentration and the lower bandgap indicates the visible-light-driven photocatalytic activity.

### 3.10 Photoluminescence studies

Fluorescence spectroscopy is conducted to inquire about the vacancies and defects inside the samples and a photoluminescence (PL) spectrum with an excitation wavelength of 420 nm at room temperature for different doping concentrations of  $\text{SnS}_2$  and Cr:  $\text{SnS}_2$  NPs and is shown in Fig. 12. Two emission peaks are observed in the PL spectra of  $\text{SnS}_2$  as well as Cr:  $\text{SnS}_2$  samples at about 562 nm and 666 nm, which are attributed to excitonic emission and the presence of surface defects, respectively [62–64]. Compared to pure  $\text{SnS}_2$ , the PL intensity decreased with Cr concentration, and doping with 1.0 at% of Cr displayed the lowest luminescence intensity, implying that additional Cr reduces defects inside the samples. This weakened luminescence intensity also indicates that a large amount of Cr substitution assists the faster separation of the photoelectron-hole pair, boosting the photocatalytic activity [40, 41].

### 3.11 Electrical properties studies of Cr: $\text{SnS}_2$ NPs

By using the two-point probe method, the electrical resistivity of  $\text{SnS}_2$  and Cr:  $\text{SnS}_2$  NPs is determined which is found to increase with Cr concentration for 0.2 at% of Cr doping, and above that point, it decreases as shown in Fig. 13a. Pristine  $\text{SnS}_2$  exhibits the minimum resistivity.

**Fig. 12** PL spectra of  $\text{SnS}_2$  and Cr:  $\text{SnS}_2$  NPs

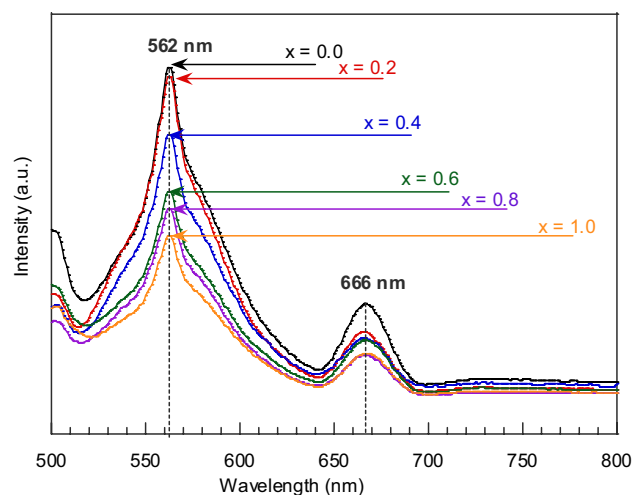


**Fig. 13** Comparison of **a** resistivity and **b** Electrical conductivity versus  $1000/T$  graphs of  $\text{SnS}_2$  and Cr:  $\text{SnS}_2$  NPs for different doping concentrations. The inset shows the variation of activation energy with Cr concentration for  $\text{SnS}_2$  and Cr:  $\text{SnS}_2$

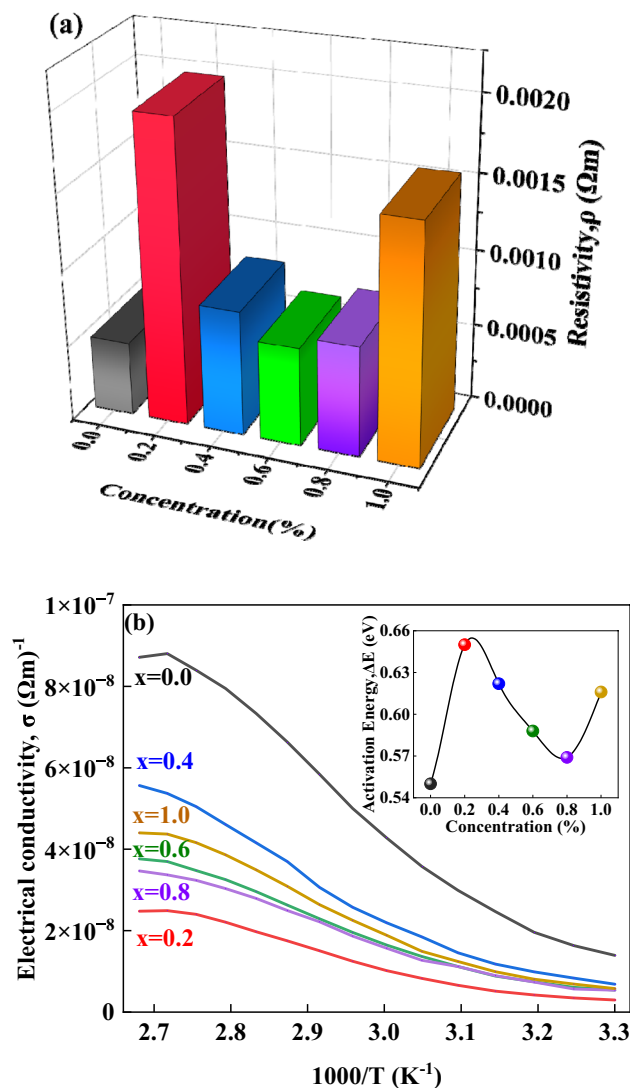


Figure 13b shows the difference in conductivity as a function of the inverse of absolute temperature for all the synthesized samples. It is evident from the graph that the conductivity of the samples increases with temperature for all six samples and varies depending on the amount of Cr. The conductivity-temperature relationship observed in Fig. 13b exhibits Arrhenius-like behavior. This behavior suggests that as the temperature rises, the mobility of charge carriers within the material improves, leading to enhanced conductivity. Undoped  $\text{SnS}_2$  shows a remarkably high conductivity of  $8.80 \times 10^{-8} (\Omega\text{m})^{-1}$ . It is evident from Fig. 13b that conductivity decreases significantly for 0.2 at % of Cr doping, after that, it increases for 0.4 at % of Cr concentration. This unusual behavior of Cr:  $\text{SnS}_2$  samples indicates the rise of structural changes of Sn, phase transition, or variations in charge carrier mobility that occur for the particular composition of tin and Cr with the increase in temperature.

The activation energies of NPs were determined from the slopes of the graph and the variation of  $E$  as a function of Cr concentration in  $\text{Sn}_{1-x}\text{Cr}_x\text{S}_2$  is shown in the inset of Fig. 13b. It is clear from the higher value of  $E$  that conductivity is extremely temperature-sensitive which might be explained by altered crystalline structure and decreased resistance of the  $\text{Sn}_{1-x}\text{Cr}_x\text{S}_2$  nanoplates.

In this study, we observed that 0.4 at% Cr doped samples exhibit the value of 0.62 eV which was significantly higher than the usual chromium-doped CIGS samples. This study highlights the importance of synthesizing NPs with the optimum composition of tin and Cr to enhance the optical and electrical properties required for desirable photovoltaic applications.

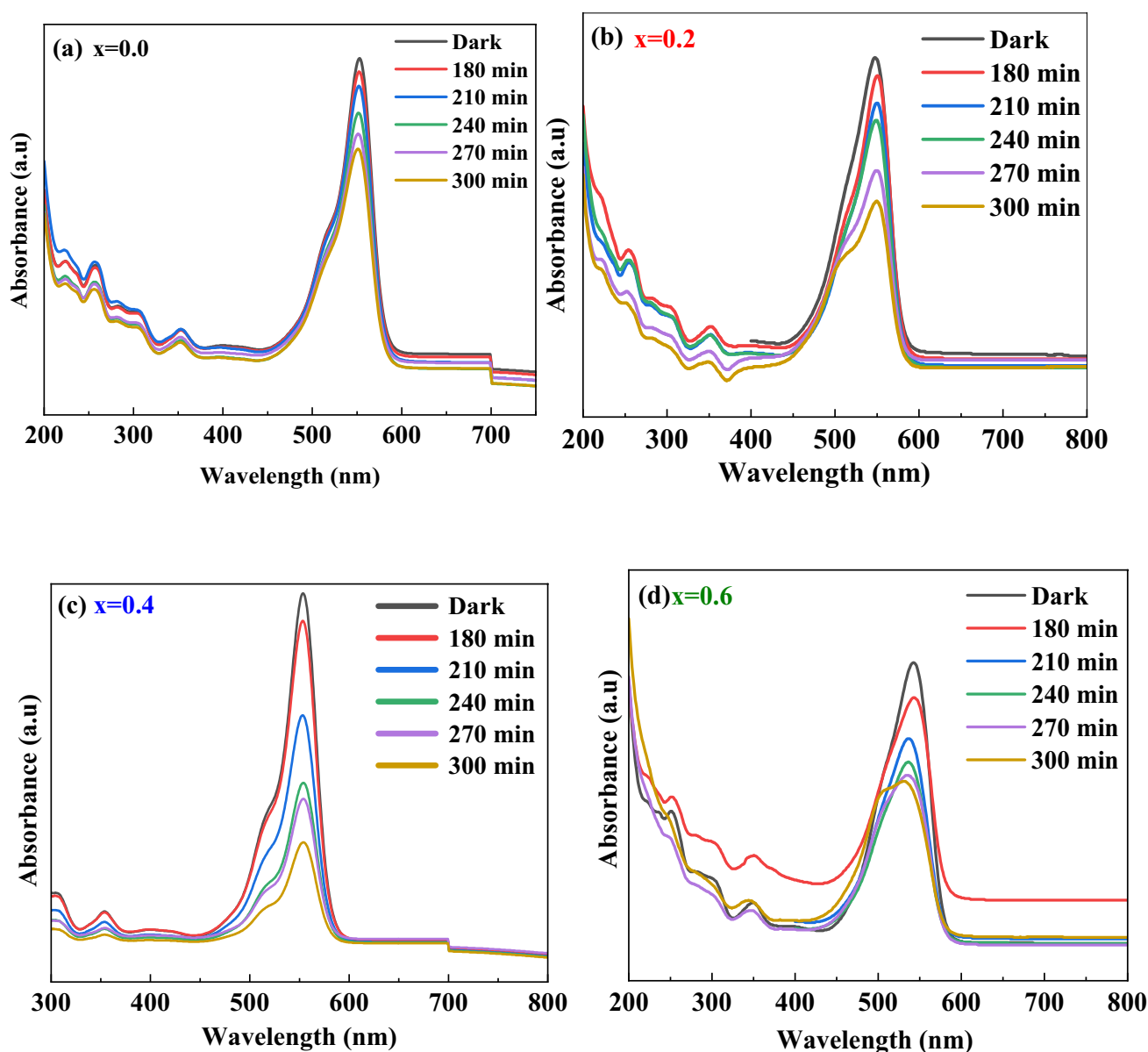
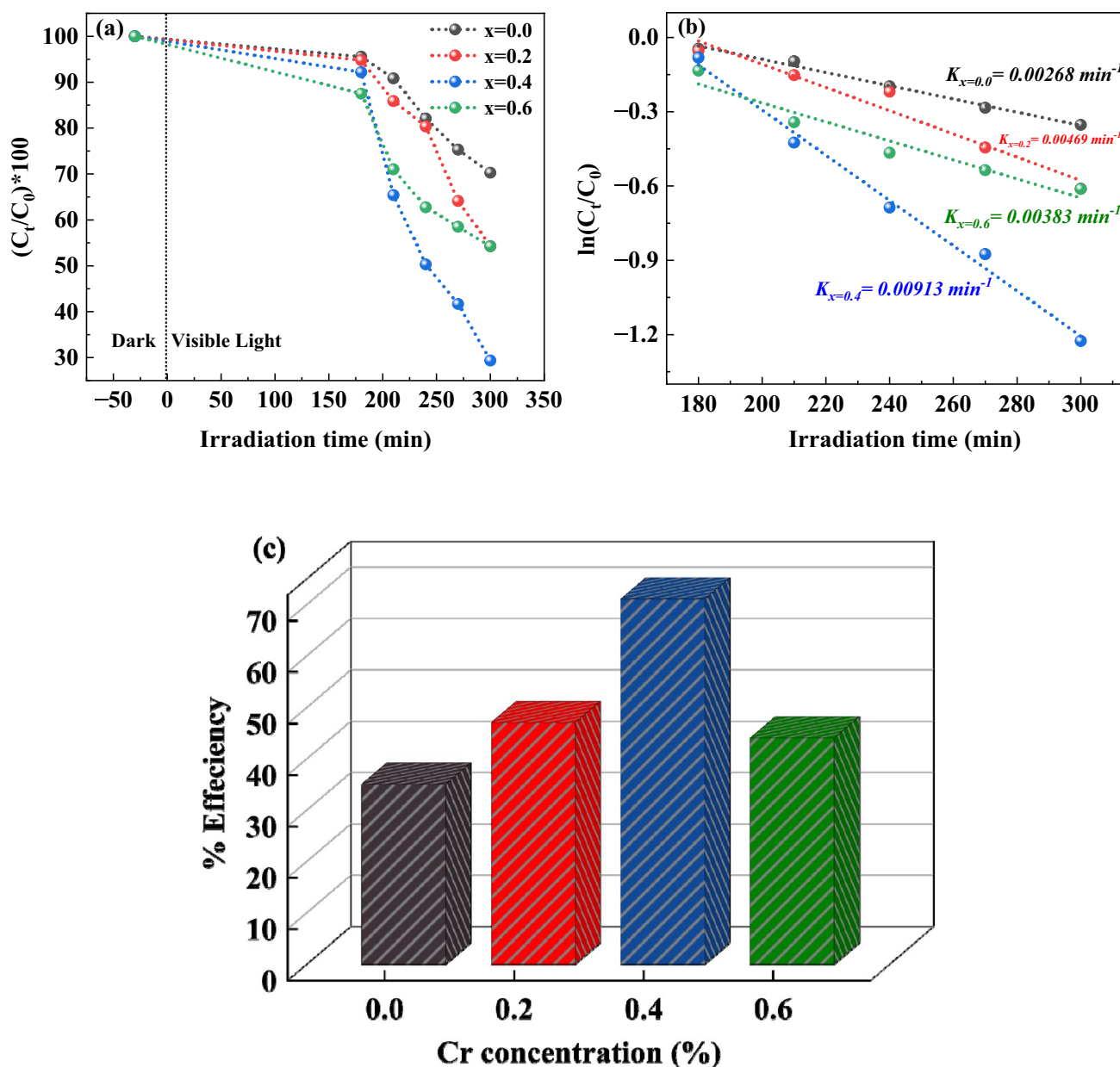


Fig. 14 UV-Vis spectral results indicating the kinetics of photoreduction of  $\text{Cr}^{3+}$  at different time intervals for **a** pure  $\text{SnS}_2$  **b** 0.2 and **c** 0.4 and **d** 0.6 at% Cr:  $\text{SnS}_2$  NPs

### 3.12 Photocatalysis analysis

Usually,  $\text{SnS}_2$  semiconductors have a d<sup>10</sup> electronic configuration which helps the detachment of photogenerated electron/hole pairs owing to the highly dispersive conduction band [21, 22, 65]. These separated charge carriers enhance the efficiency of  $\text{SnS}_2$  as a visible light-driven photocatalyst. The photocatalytic activity of prepared pure  $\text{SnS}_2$  and Cr:  $\text{SnS}_2$  nanoplates was evaluated by the degradation of rhodamine B (RhB) dye under visible light ( $\lambda \geq 420$  nm) irradiation at room temperature.

Figure 14a–d shows the sequential change in the absorbance spectra (200 to 800 nm) of rhodamine B (RhB) with prepared nanoplates photocatalysis in regular time intervals under visible light irradiation. From the figures, the nanoplates catalyst was observed to degrade RhB in visible light by showing the decolorization. The photocatalytic degradation was recorded at wavelengths of 554 nm and a trend of weakening of the absorption intensity is observed



**Fig. 15** Plots of **a** degradation of RhB over time with SnS<sub>2</sub> and Cr: SnS<sub>2</sub> NPs **b**  $\ln(C_t/C_0)$  versus irradiation time corresponding to first-order kinetics of degradation of RhB and **c** % efficiency for different Cr concentration

with the increasing exposure time under visible light irradiation for the nanoplates catalysts. The decolorization of RhB of SnS<sub>2</sub> and Cr: SnS<sub>2</sub> NPs nanoplates considerably rises with an increase in Cr doping.

The relative concentration of RhB has been analyzed by monitoring the RhB absorption peak at 554 nm in the absence and presence of visible light irradiation using SnS<sub>2</sub> and Cr: SnS<sub>2</sub> NPs, as shown in Fig. 15a. It is evident from the graph that in the absence of visible light irradiation (during the initial 30 min), the degradation rate of RhB was almost negligible for all the samples.

The first-order kinetics of Cr: SnS<sub>2</sub> NPs for photocatalytic decolorization of RhB can be expressed by the equation [23, 28, 52]:  $\ln(C_t/C_0) = kt$ , where  $C_t$  and  $C_0$  are the concentrations after  $t$  irradiation time (min) and initial concentrations of RhB at the dark adsorption equilibrium ( $t = 0$ ), and  $k$  represents the reaction rate constant of the first order ( $\text{min}^{-1}$ ). The  $k$  values of the photocatalytic decolorization rates of NPs are shown in Fig. 15b. It is found that the rate constant  $k$  values of 0.4 at% Cr: SnS<sub>2</sub> NPs has the highest value ( $0.00913 \text{ min}^{-1}$ ), which is 3.4 times that of pure SnS<sub>2</sub> ( $0.00268 \text{ min}^{-1}$ ). The higher  $k$  value demonstrates that Cr doping increases the photocatalytic efficiency of SnS<sub>2</sub> NPs by altering



the energy band structure to raise the electron–hole pairs separation. After that, the photocatalytic activity decreases with the increase of the doping concentration for 0.6 at% Cr: SnS<sub>2</sub> NPs which might be attributed to the increase in the electron–hole recombination probability.

Then the concentration of RhB degraded up to 35%, 47%, 71%, and 44% at 300 min respectively for pure SnS<sub>2</sub>, 0.2, 0.4, and 0.6 at% Cr: SnS<sub>2</sub> NPs as shown in Fig. 15c. It was found from the degradation data that the best catalytic performance was achieved by Sn<sub>0.6</sub>Cr<sub>0.4</sub>S<sub>2</sub> photocatalyst which exhibits the highest decolorization rate at 71% after 300 min of visible light irradiation. Many factors such as crystallite size, band gap, specific surface area, morphology, and crystal defects dominate the photocatalytic activity of Cr: SnS<sub>2</sub> NPs [24, 27, 66]. Probably the 0.4 at% Cr: SnS<sub>2</sub> NPs exhibit more adsorption sites for exposure to the sunlight, increasing the photocatalytic activity. Moreover, the higher catalytic activity of 0.4 at% Cr: SnS<sub>2</sub> NPs might be associated with their smaller crystallite size, higher surface area, and relevant band gap.

This work tested 0.4 at% Cr: SnS<sub>2</sub> reusability in five cycles of catalytic degradation of RhB under visible light irradiation. After every cycle, the photocatalyst was retrieved from the suspension by centrifugal separation, and washed with ethanol and deionized water for three times to remove the residual organic species. Then the suspension was dried in an oven at 70 °C for 12 h and reused for the next cycle. From Fig. 16a, a small decrease in photocatalytic degradation efficiency (~7%) was observed after five cycles of photocatalytic application due to the loss of sample during the preparation of the cycling process. Moreover, the XRD pattern of retrieved 0.4 at% Cr: SnS<sub>2</sub> after the reuse experiment exhibits the same crystal structure as that of the as-prepared 0.4 at% Cr: SnS<sub>2</sub> shown in Fig. 16b which clearly indicates the good photocatalytic reusability of 0.4 at% Cr: SnS<sub>2</sub>.

The photocatalyst activity relies on the intensity of incident light, the concentration of the photocatalyst, the pollutant's initial concentration, the generation of charge carriers, and active oxidizing agents. In the case of using transition metal doped semiconductor nano-photocatalysts, transition metal ions' effect on the photocatalysis reaction rate and the transformation of metal ions to less toxic species need to be considered. Based on the prior results, the schematic mechanism of the

**Fig. 16** **a** Affirmation of reusability of 0.4% Cr: SnS<sub>2</sub> catalyst for the degradation of RhB dye up to the fifth cycles; **b** XRD patterns of the as-prepared and reused (five times) Cr: SnS<sub>2</sub> NPs

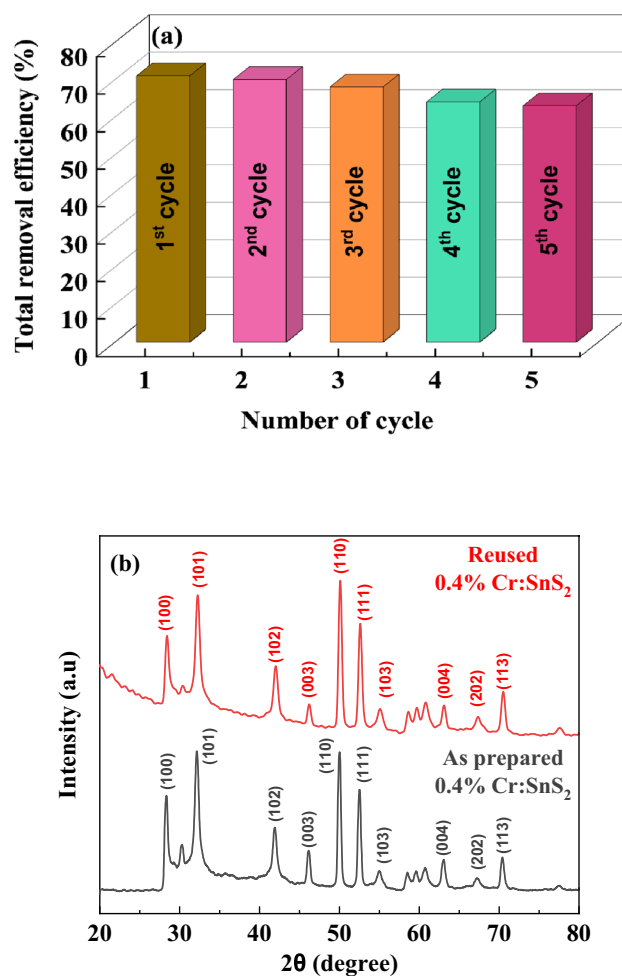
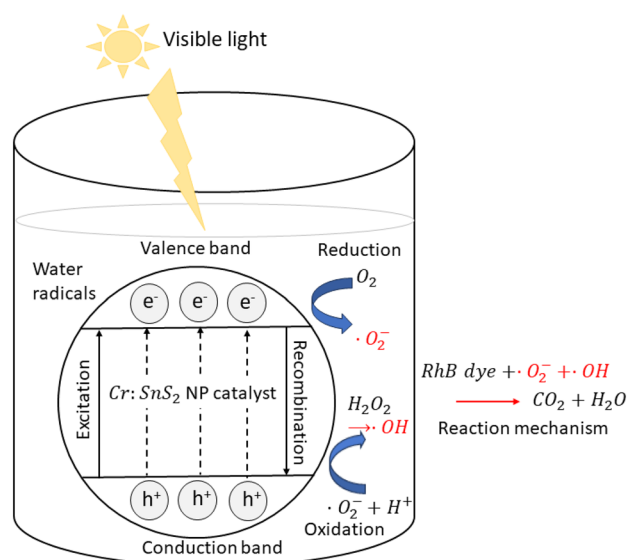
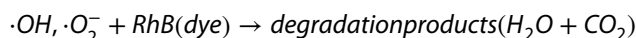
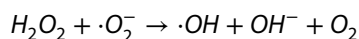
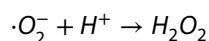
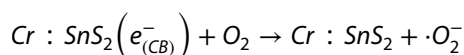
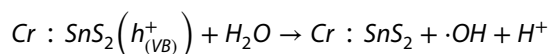
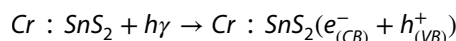


**Fig. 17** Photocatalytic mechanism of Cr: SnS<sub>2</sub> NPs



photocatalytic activity of Cr-doped SnS<sub>2</sub> nanoplates is proposed in Fig. 17. During the photocatalysis experiment of Cr-doped SnS<sub>2</sub> nanoplates, the reactions that occurred in the degradation of RhB under visible light may be expressed as the following:



When pure SnS<sub>2</sub> and Cr: SnS<sub>2</sub> are exposed under visible light irradiation, the electrons from the valence band (VB) are excited to its conduction band (CB) and start to produce electron and hole pairs which can recombine or interact with other molecules. The produced electron (e<sub>(CB)</sub><sup>-</sup>) and hole (h<sub>(VB)</sub><sup>+</sup>) from CB and VB respectively migrate toward the photocatalyst surface to interact with the dye solution and anticipated oxidation–reduction reactions. The electrons react with the oxygen molecules attached over the photocatalyst surface to form superoxide anion radicals (·O<sub>2</sub><sup>-</sup>) and the hole reacts with the hydroxyl groups of the water molecules to form highly reactive hydroxyl radicals (·OH). Concurrently, superoxide anion radicals (·O<sub>2</sub><sup>-</sup>) react with proton and forms H<sub>2</sub>O<sub>2</sub> which later disintegrates into hydroxyl radicals (·OH) [65]. Finally, superoxide anion radicals (·O<sub>2</sub><sup>-</sup>) and hydroxyl radicals (·OH) react with the RhB dye and transform it into less toxic chemicals CO<sub>2</sub>, and H<sub>2</sub>O. Compared with SnS<sub>2</sub>, Cr: SnS<sub>2</sub> nanoplates have possessed better photocatalytic efficiency as quantum effects of transition metal nanoparticles cause local surface plasmon resonance (LSPR) and produce more electron and hole pairs.

## 4 Conclusion

Pure SnS<sub>2</sub> and Cr: SnS<sub>2</sub> nanoplates with various Cr concentrations (0.2, 0.4, 0.6, 0.8, 1 at %) were successfully prepared via hydrothermal method using HCl as a stabilizer. All the samples exhibit hexagonal crystal structure and Cr doping increased the lattice parameters of the SnS<sub>2</sub> NPs. The pristine SnS<sub>2</sub> and Cr: SnS<sub>2</sub> NPs displayed hexagonal-like nanosheets

with smooth, vertically interconnected surfaces. As the mole percentage of Cr increases, the particle size becomes larger, and agglomerates also consist of a mixture of more fine grains with sizes in the range of 140 to 340 nm diameter. The survey spectrum shows that the produced nanoplates incorporate Sn, S, and Cr elements in  $\text{Sn}^{4+}$ ,  $\text{S}^{2-}$ , and  $\text{Cr}^{3+}$  states. Cr doped promotes the formation of Dilute magnetic semiconductors by introducing ferromagnetic order in the  $\text{SnS}_2$  which can be used in the spintronic devices. UV–Vis and PL spectra indicate the excitonic absorptions and emissions from the  $\text{SnS}_2$  NPs. The PL intensity shows that doping with 1.0 at% of Cr displayed the lowest luminescence intensity, implying that additional Cr reduces defects inside the samples. Moreover, Pristine  $\text{SnS}_2$  exhibits the minimum resistivity and a higher value of activation energy indicating that conductivity is extremely temperature-sensitive which might be explained by altered crystalline structure and decreased resistance of the  $\text{Sn}_{1-x}\text{Cr}_x\text{S}_2$  nanoplates. The  $\text{SnS}_2$  and Cr:  $\text{SnS}_2$  NPs exhibit remarkable photocatalytic activity. Cr:  $\text{SnS}_2$  NPs degrade RhB under visible light irradiation. It should be highlighted that the  $\text{Sn}_{0.6}\text{Cr}_{0.4}\text{S}_2$  photocatalyst exhibits the highest rate of decolorization at 71% which is 3.4 times higher with compared to pure  $\text{SnS}_2$  catalyst.

**Acknowledgements** The authors gratefully acknowledge to Materials Science Division, Atomic Energy Centre, Dhaka, and Bangladesh Council of Scientific and Industrial Research for extending the use of experimental facilities. We also thank the Centre for Advanced Research of Sciences (CARS), Semiconductor Technology Research Centre (STRC), University of Dhaka, and Nano and Advanced Materials Laboratory, Department of Physics, University of Dhaka, for their cooperation while carrying out this research.

**Author contributions** Conceptualization: Kazi Haniem Maria; Methodology: Aparna Paul, Rutaba Jania and Kazi Haniem Maria; Formal analysis and investigation: Aparna Paul, Rutaba Jania and Kazi Haniem Maria; Writing—original draft preparation: Kazi Haniem Maria, Aparna Paul; Writing—review and editing: Kazi Haniem Maria, Aparna Paul and I. N. Esha; Resources: Sheikh Manjura Hoque, Shirin Akter Jahan, Faria Chowdhury; Supervision: Kazi Haniem Maria.

**Funding** This investigation was financially supported by the Special Allocation grant from the Ministry of Science and Technology (2023–2024).

**Data availability** The supported data of the research findings are available from the corresponding author upon reasonable request.

**Code availability** Not applicable.

## Declarations

**Competing interests** The authors declare no competing interests.

**Open Access** This article is licensed under a Creative Commons Attribution-NonCommercial-NoDerivatives 4.0 International License, which permits any non-commercial use, sharing, distribution and reproduction in any medium or format, as long as you give appropriate credit to the original author(s) and the source, provide a link to the Creative Commons licence, and indicate if you modified the licensed material. You do not have permission under this licence to share adapted material derived from this article or parts of it. The images or other third party material in this article are included in the article's Creative Commons licence, unless indicated otherwise in a credit line to the material. If material is not included in the article's Creative Commons licence and your intended use is not permitted by statutory regulation or exceeds the permitted use, you will need to obtain permission directly from the copyright holder. To view a copy of this licence, visit <http://creativecommons.org/licenses/by-nc-nd/4.0/>.

## References

1. Sun Y, Xia Y. Shape-controlled synthesis of gold and silver nanoparticles. *Science*. 2002;298:2176–9. <https://doi.org/10.1126/science.1077229>.
2. Maillard M, Giorgio S, Pilen MP. Tuning the size of silver nanodisks with similar aspect ratios: synthesis and optical properties. *J Phys Chem B*. 2003;107:2466–70. <https://doi.org/10.1021/jp022357q>.
3. Mohan K, Lakshmanan VR. A critical review of the recent trends in source tracing of microplastics in the environment. *Environ Res*. 2023;239: 117347. <https://doi.org/10.1016/j.envres.2023.117394>.
4. Alivisatos AP. Semiconductor clusters, nanocrystals, and quantum dots. *Science*. 1996;271:933–7. <https://doi.org/10.1126/science.271.5251.933>.
5. Li M, Schnablegger H, Mann S. Coupled synthesis and self-assembly of nanoparticles to give structures with controlled organization. *Nature*. 1999;402:393–5. <https://doi.org/10.1038/46509>.
6. Cui Y, Lieber CM. Functional nanoscale electronic devices assembled using silicon nanowire building blocks. *Science*. 2001;291:851–3. <https://doi.org/10.1126/science.291.5505.851>.
7. Mitzi DB, Kosbar LL, Murray CE, Copel M, Afzali A. High-mobility ultrathin semiconducting films prepared by spin coating. *Nature*. 2004;428:299–303. <https://doi.org/10.1038/nature02389>.
8. Kumar S, Nann T. Shape control of II–VI semiconductor nanomaterials. *Small*. 2006;2:316–29. <https://doi.org/10.1002/smll.200500357>.

9. Zhang YC, Yao L, Zhang G, Dionysiou DD, Li J, Du X. One-step hydrothermal synthesis of high-performance visible-light-driven SnS<sub>2</sub>/SnO<sub>2</sub> nanoheterojunction photocatalyst for the reduction of aqueous Cr(VI). *Appl Catal B*. 2014;144:730–8. <https://doi.org/10.1016/j.apcatb.2013.08.006>.
10. Gogoi HP, Bisoi G, Barman P, Dehingia A, Das S, Chowdhury AP. Highly efficient and recyclable quaternary Ag/Ag<sub>3</sub>PO<sub>4</sub>-BiOBr-C<sub>3</sub>N<sub>4</sub> composite fabrication for efficient solar-driven photocatalytic performance for anionic pollutant in an aqueous medium and mechanism insights. *Opt Mater*. 2023;138: 113712. <https://doi.org/10.1016/j.optmat.2023.113712>.
11. Chowdhury AP, Shambharkar BH. Synthesis and characterization of BiOCl-Cu<sub>2</sub>ZnSnS<sub>4</sub> heterostructure with enhanced photocatalytic activity. *Appl Water Sci*. 2018;8:202. <https://doi.org/10.1007/s13201-018-0853-0>.
12. Chowdhury AP, Anantharaju KS, Umare SS, Dhar SS. Facile fabrication of binary BiOCl-Cu<sub>2</sub>CoSnS<sub>4</sub> and ternary BiOCl-Cu<sub>2</sub>CoSnS<sub>4</sub>-TiO<sub>2</sub> heterojunction nano photocatalyst for efficient sunlight-driven removal of direct blue 71 in an aqueous medium. *Colloids Surf, A*. 2022;652: 129841. <https://doi.org/10.1016/j.colsurfa.2022.129841>.
13. Zhao W, Wei Z, Zhang L, Wu X, Wang X. Cr doped SnS<sub>2</sub> nanoflowers: preparation, characterization and photocatalytic decolorization. *Mater Sci Semicond Process*. 2018;88:173–80. <https://doi.org/10.1016/j.msssp.2018.08.011>.
14. Wannapop S, Somdee A. Highly orientated one-dimensional Cu<sub>2</sub>O/TiO<sub>2</sub> heterostructure thin film for photoelectrochemical photoanode and photocatalytic degradation applications. *Thin Solid Films*. 2022;747: 139144. <https://doi.org/10.1016/j.tsf.2022.139144>.
15. Rehman S, Ullah R, Butt AM, Gohar ND. Strategies of making TiO<sub>2</sub> and ZnO visible light active. *J Hazard Mater*. 2009;170:560–9. <https://doi.org/10.1016/j.jhazmat.2009.05.064>.
16. Somdee A, Wannapop S. Enhanced photocatalytic behavior of ZnO nanorods decorated with a Au, ZnWO<sub>4</sub>, and Au/ZnWO<sub>4</sub> composite: synthesis and characterization. *Colloid Interface Sci Commun*. 2022;47: 100591. <https://doi.org/10.1016/j.colcom.2022.100591>.
17. Limsakul S, Mahatnirunkul T, Phromma C, Chomtong T, Cholnakasem N, Yimklan S, Ruankham P, Siyasukh A, Chimupala Y. Novel physical sunscreen from one-dimensional TiO<sub>2</sub> nanowire: synthesis, characterization and the effects of morphologies and particle size for use as a physical sunscreen. *Nano-Struct Nano-Objects*. 2023;35: 101027. <https://doi.org/10.1016/j.nanoso.2023.101027>.
18. Julien CM, Eddrief M, Samaras I, Balkanski M. Optical and electrical characterizations of SnSe, SnS<sub>2</sub>, and SnSe<sub>2</sub> single crystals. *Mater Sci Eng, B*. 1992;15:70–2. [https://doi.org/10.1016/0921-5107\(92\)90033-6](https://doi.org/10.1016/0921-5107(92)90033-6).
19. Das NS, Roy A, Chowdhury A. Optical and structural studies of tin disulfide (SnS<sub>2</sub>) synthesized by facile hydrothermal method. *Lett Appl NanoBioSci*. 2023;12:47. <https://doi.org/10.33263/LIANBS122.047>.
20. Stengl V, Bakardjieva S, Grygar TM, Bludská J, Kormunda M. TiO<sub>2</sub>-graphene oxide nanocomposite as advanced photocatalytic materials. *Chem Cent J*. 2013;7:41. <https://doi.org/10.1186/1752-153X-7-41>.
21. Maria KH, Kabir R, Esha IN, Toma FTZ, Bashar MS, Hussain KA. Characterization of tin disulfide thin films prepared by spin coating technique: effect of spin speed and deposition time on film properties. *Trans Indian Inst Met*. 2023;76:2709–20. <https://doi.org/10.1007/s12666-023-02968-4>.
22. Maria KH, Sakhujia N, Jha RK, Bhat N. Ultra-sonication assisted synthesis of 2D SnS<sub>2</sub> nanoflakes for room-temperature no gas detection. *IEEE Sens J*. 2021;21:10420–7. <https://doi.org/10.1109/JSEN.2021.3059087>.
23. Wang Y, Su Y, Fang W, Zhang Y, Li X, Zhang G, Sun W. SnO<sub>2</sub>/SnS<sub>2</sub> nanocomposite anchored on nitrogen-doped RGO for improved photocatalytic reduction of aqueous Cr(VI). *Powder Technol*. 2020;363:337–48. <https://doi.org/10.1016/j.powtec.2020.01.009>.
24. Zhang Y, Zhang F, Yang Z, Xue H, Dionysiou DD. Development of a new efficient visible-light-driven photocatalyst from SnS<sub>2</sub> and polyvinyl chloride. *J Catal*. 2016;344:692–700. <https://doi.org/10.1016/j.jcat.2016.10.022>.
25. Hong SY, Popovitz-Biro R, Prior Y, Tenne R. Synthesis of SnS<sub>2</sub>/SnS fullerene-like nanoplates: a superlattice with polyhedral shape. *J Am Chem Soc*. 2003;125:10470–4. <https://doi.org/10.1021/ja036057d>.
26. Hai B, Tang K, Wang C, An C, Yang Q, Shen G, Qian Y. Synthesis of SnS<sub>2</sub> nanocrystals via a solvothermal process. *J Cryst Growth*. 2001;225:92–5. [https://doi.org/10.1016/S0022-0248\(01\)01030-2](https://doi.org/10.1016/S0022-0248(01)01030-2).
27. Chen D, Shen G, Tang K, Liu Y, Qian Y. Aligned SnS<sub>2</sub> nanotubes fabricated via a template-assisted solvent-relief process. *Appl Phys A*. 2003;77:747–9. <https://doi.org/10.1007/S00339-003-2215-4>.
28. Zhang F, Shen L, Li J, Zhang Y, Wang G, Zhu A. Room temperature photocatalytic deposition of Au nanoparticles on SnS<sub>2</sub> nanoplates for enhanced photocatalysis. *Powder Technol*. 2021;383:371–80. <https://doi.org/10.1016/j.powtec.2021.01.065>.
29. Zhang F, Zhang Y, Zhang G, Yang Z, Dionysiou DD, Zhu A. Exceptional synergistic enhancement of the photocatalytic activity of SnS<sub>2</sub> by coupling with polyaniline and N-doped reduced graphene oxide. *Appl Catal B*. 2018;236:53–63. <https://doi.org/10.1016/j.apcatb.2018.05.002>.
30. Zhang F, Zhang Y, Wang Y, Zhu A, Zhang Y. Efficient photocatalytic reduction of aqueous Cr (VI) by Zr<sup>4+</sup> doped and polyaniline coupled SnS<sub>2</sub> nanoflakes. *Sep Purif Technol*. 2022;283: 120161. <https://doi.org/10.1016/j.seppur.2021.120161>.
31. Yang Q, Tang K, Wang C, Zhang D, Qian Y. The synthesis of SnS<sub>2</sub> nanoplates from tetrabutyltin precursor. *J Solid State Chem*. 2002;164:106–9. <https://doi.org/10.1006/jssc.2001.9453>.
32. Lei Y, Song S, Fan W, Xing Y, Zhang H. Facile synthesis and assemblies of flowerlike SnS<sub>2</sub> and In<sup>3+</sup>-doped SnS<sub>2</sub>: hierarchical structures and their enhanced photocatalytic property. *J Phys Chem C*. 2009;113:1280–5. <https://doi.org/10.1021/jp8079974>.
33. Kiruthigaa G, Manoharan C, Raju C, Dhanapandian S, Thanikachalam V. Synthesis and spectroscopic analysis of undoped and Zn doped SnS<sub>2</sub> nanostructure by solid-state reaction method. *Mater Sci Semicond Process*. 2014;26:533–9. <https://doi.org/10.1016/j.msssp.2014.05.048>.
34. Kiruthigaa G, Manoharan C, Bououdina M, Ramalingam S, Raju C. Structural, optical and photocatalytic properties of Ce-doped SnS<sub>2</sub> nanoflakes. *Solid State Sci*. 2015;44:32–8. <https://doi.org/10.1016/j.solidstatesciences.2015.04.003>.
35. Wang N, Wu P, Sun L, Zhou W. Ferromagnetic spin-order in Mg-doped SnS<sub>2</sub> nanoflowers prepared by hydrothermal method. *J Phys Chem Solids*. 2016;92:1–6. <https://doi.org/10.1016/j.jpcs.2016.01.011>.
36. Chen A, Xia S, Pan X, Lu H, Ji Z. Easily removable visible-light-driven photocatalyst of nickel modified SnS<sub>2</sub> nanosheets for reduction of Cr(VI). *J Alloy Compd*. 2018;735:1314–8. <https://doi.org/10.1016/j.jallcom.2017.10.248>.
37. Park S, Selvaraj R, Meetani MA, Kim Y. Enhancement of visible-light-driven photocatalytic reduction of aqueous Cr(VI) with flower-like In<sup>3+</sup>-doped SnS<sub>2</sub>. *J Ind Eng Chem*. 2017;45:206–14. <https://doi.org/10.1016/j.jiec.2016.09.024>.

38. Jiang M, Huang Y, Sun W, Zhang X. Co-doped SnS<sub>2</sub> nanosheet array for efficient oxygen evolution reaction electrocatalyst. *J Mater Sci.* 2019;54:13715–23. <https://doi.org/10.1007/s10853-019-03856-3>.
39. Ullah S, Bouich A, Ullah H, Mari B, Mollar M. Enhanced optical and structural properties of V-doped binary SnS<sub>2</sub> buffer layer. *Sol Energy.* 2020;20:654–9. <https://doi.org/10.1016/j.solener.2020.04.095>.
40. Ullah S, Ullah H, Parra SG, Andrio A, Mari B, Compan V. Improvement of optical and conductivity properties of SnS<sub>2</sub> via Cr doping for photovoltaic applications. *J Alloy Compd.* 2023;960: 171047. <https://doi.org/10.1016/j.jallcom.2023.171047>.
41. Zhang L, Ge S, Zuo Y, Wang J, Qi J. Ferromagnetic properties in undoped and Cr-doped SnO<sub>2</sub> nanowires. *Scripta Mater.* 2010;63:953–6. <https://doi.org/10.1016/j.scriptamat.2010.06.025>.
42. Lin L, Chen Y, Tao H, Yao L, Huang J, Zhu L, Lou M, Chen R, Yana L, Zhang Z. Ferromagnetism and optical properties of SnS<sub>2</sub> doped with two impurities: first-principles calculations. *Phys Chem Chem Phys.* 2021;23:6574–82. <https://doi.org/10.1039/D0CP06322C>.
43. Matyszczak G, Jozwik P, Polesiak E, Sobieska M, Krawczyk K, Jastrzębski C, Plocinski T. Sonochemical preparation of SnS and SnS<sub>2</sub> nano- and micropowders and their characterization. *Ultrason Sonochem.* 2021;75: 105594. <https://doi.org/10.1016/j.ultsonch.2021.105594>.
44. Ahmad H, Kamarudin SK, Minggu LJ, Kassim M. Hydrogen from photo-catalytic water splitting process: a review. *Renew Sustain Energy Rev.* 2015;43:599–610. <https://doi.org/10.1016/j.rser.2014.10.101>.
45. Damkale SR, Arbutj SS, Umarji GG, Panmand RP, Khore SK, Sonawane RS, Rane SB, Kale BB. Two dimensional hexagonal SnS<sub>2</sub> nanostructures for photocatalytic hydrogen generation and dye degradation. *Sustain Energy Fuels.* 2019;3:3406–14. <https://doi.org/10.1039/C9SE00235A>.
46. Phillips R, Jolley K, Zhou Y, Smith R. Influence of temperature and point defects on the X-ray diffraction pattern of graphite. *Carbon Trends.* 2021;5: 100124. <https://doi.org/10.1016/j.cartre.2021.100124>.
47. Gaur R, Jeevanandam P. Synthesis of SnS<sub>2</sub> nanoplates and their application as photocatalysts for the reduction of Cr(VI). *J Nanosci Nanotechnol.* 2018;18:165–77. <https://doi.org/10.1166/jnn.2018.14604>.
48. Luo J, Zhou X, Ma L, Xu L, Xu X, Du Z, Zhang J. Enhancing visible light photocatalytic activity of direct Z-scheme SnS<sub>2</sub>/Ag<sub>3</sub>PO<sub>4</sub> heterojunction photocatalysts. *J Mater Sci.* 2016;81:16–26. <https://doi.org/10.1016/j.materresbull.2016.04.028>.
49. Zhang YC, Li J, Xu HY. One-step in situ solvothermal synthesis of SnS<sub>2</sub>/TiO<sub>2</sub> nanocomposites with high performance in visible light-driven photocatalytic reduction of aqueous Cr(VI). *Appl Catal B.* 2012;123:18–26. <https://doi.org/10.1016/j.apcatb.2012.04.018>.
50. Fu W, Wang J, Zhou S, Li R, Peng T. Controllable fabrication of regular hexagon-shaped SnS<sub>2</sub> nanoplates and their enhanced visible-light-driven H<sub>2</sub> production activity. *ACS Appl Nano Mater.* 2018;1:2923–33. <https://doi.org/10.1021/acsanm.8b00563>.
51. Chaki SH, Deshpande MP, Trivedi DP, Tailor JP, Chaudhary MD, Mahato K. Wet chemical synthesis and characterization of SnS<sub>2</sub> nanoplates. *Appl Nanosci.* 2013;3:189–95. <https://doi.org/10.1007/s13204-012-0123-7>.
52. Zou W, Sun LH, Cong SN, Leng RX, Zhang Q, Zhao L, Kang SZ. Preparation of worm-like SnS<sub>2</sub> nanoplates and their photocatalytic activity. *J Exp Nanosci.* 2020;15:100–8. <https://doi.org/10.1080/17458080.2020.1750600>.
53. Gajendiran J, Rajendiran V. Synthesis of SnS<sub>2</sub> nanoplates by a surfactant-mediated hydrothermal method and their characterization. *Adv Nat Sci Nanosci Nanotechnol.* 2011;2: 015001. <https://doi.org/10.1088/2043-6262/2/1/015001>.
54. Voznyi A, Kosyak V, Opanasyuk A, Tirkusova N, Grase L, Medvids A, Mezinskis G. Structural and electrical properties of SnS<sub>2</sub> thin films. *Mater Chem Phys.* 2016;173:52–61. <https://doi.org/10.1016/j.matchemphys.2016.01.036>.
55. Mukherjee A, Mitra P. Characterization of tin (II) sulphide thin film synthesized by successive chemical solution deposition. *Indian J Phys.* 2015;89:1007–12. <https://doi.org/10.1007/s12648-015-0673-0>.
56. Reena RS, Aslinjensipriya A, Jose M, Das SJ. Investigation on structural, optical and electrical nature of pure and Cr-incorporated cobalt oxide nanoplates prepared via co-precipitation method for photocatalytic activity of methylene blue dye. *J Mater Sci: Mater Electron.* 2020;31:22057–74. <https://doi.org/10.1007/s10854-020-04708-6>.
57. Gedi S, Alhammadi S, Noh J, Minnam VR, Park H, Rabie AM, Shim J, Kang D, Kim WK. SnS<sub>2</sub> nanoplates and thin film for application as an adsorbent and photovoltaic buffer. *Nanomaterials.* 2022;12:1–13. <https://doi.org/10.3390/nano12020282>.
58. Huang X, Chen J, Xu F. Structural and magnetic properties of Fe-doped SnS<sub>2</sub> nanopowders synthesized by solid-state reaction method. *Chem Phys Lett.* 2020;739: 137042. <https://doi.org/10.1016/j.cplett.2019.137042>.
59. Khimani AJ, Chaki SH, Chauhan SM, Mangrola AV, Meena R, Deshpande MP. Synthesis, characterization, antimicrobial and antioxidant study of the facile sonochemically synthesized SnS<sub>2</sub> nanoparticles. *Nano-Struct Nano-Objects.* 2019;18: 100286. <https://doi.org/10.1016/j.nanos.2019.100286>.
60. Li B, Xing T, Zhong M, Huang L, Lei N, Zhang J, Li J, Wei Z. A two-dimensional Fe-doped SnS<sub>2</sub> magnetic semiconductor. *Nat Commun.* 2017;8:1–7. <https://doi.org/10.1038/s41467-017-02077-z>.
61. Chaki SH, Mahato KS, Malek TJ, Deshpande MP. CuAlS<sub>2</sub> thin films—dip coating deposition and characterization. *J Sci Adv Mater Devices.* 2017;2:215–24. <https://doi.org/10.1016/j.jsamd.2017.04.002>.
62. Nath D, Singh F, Das R. X-ray diffraction analysis by Williamson-Hall, Halder-Wagner, and size-strain plot methods of CdSe nanoplates—a comparative study. *Mater Chem Phys.* 2020;239: 122021. <https://doi.org/10.1016/j.matchemphys.2019.122021>.
63. Arulanantham AMS, Valanarasa S, Kathalingam A, Jeyadheepan K. Influence of carrier gas pressure on nebulizer spray deposited tin disulfide thin films. *J Mater Sci: Mater Electron.* 2018;29:11358–66. <https://doi.org/10.1007/s10854-018-9223-9>.
64. S. Mohebbi, P. Askari, R. Rashidi. Magnetic and optical properties of Fe doped SnS nanoplates with zinc blende structure. *Int J Adv Sci Eng Technol.* 2018; 6: 52–55. Online No—IJASEAT-IRAJ-ONLINE-11656
65. Mondal C, Ganguly M, Pal J, Roy A, Jana J, Pal T. Morphology controlled synthesis of SnS<sub>2</sub> nanomaterial for promoting photocatalytic reduction of aqueous Cr(VI) under visible light. *Langmuir.* 2014;30:4157–64. <https://doi.org/10.1021/la500509c>.
66. Wang X, Ren P, Fan H. Room-temperature solid state synthesis of ZnO/Bi<sub>2</sub>O<sub>3</sub> heterojunction and their solar light photocatalytic performance. *Mater Res Bull.* 2015;64:82–7. <https://doi.org/10.1016/j.materresbull.2014.12.037>.